END

FILMED

DTIC

MICROCOPY RESOLUTION TEST CHART
NATIONAL BUREAU OF STANDARDS-1963-A

⑫

REPORT DOCUMENTATION PAGE	READ INSTRUCTIONS BEFORE COMPLETING FORM

1. REPORT NUMBER 7 -5	2. GOVT ACCESSION NO. AD /122 /37	3. RECIPIENT'S CATALOG NUMBER

4. TITLE (and Subtitle)	5. TYPE OF REPORT & PERIOD COVERED
SCF-Xα-SW Cluster Molecular-Orbital Models of Catalysts, Alloys, Magnetic Materials, and Superconductors	Interim
	6. PERFORMING ORG. REPORT NUMBER

7. AUTHOR(s)	8. CONTRACT OR GRANT NUMBER(s)
K. H. Johnson	NC0014-81-K-0499

9. PERFORMING ORGANIZATION NAME AND ADDRESS	10. PROGRAM ELEMENT, PROJECT, TASK AREA & WORK UNIT NUMBERS
Center for Materials Science and Engineering, M.I.T., Cambridge, Massachusetts 02139	Task No. Nr 056-757

11. CONTROLLING OFFICE NAME AND ADDRESS	12. REPORT DATE
Office of Naval Research Department of the Navy Arlington, Virginia 22217	November 29, 1982
	13. NUMBER OF PAGES 48

14. MONITORING AGENCY NAME & ADDRESS(if different from Controlling Office)	15. SECURITY CLASS. (of this report)
	15a. DECLASSIFICATION/DOWNGRADING SCHEDULE

16. DISTRIBUTION STATEMENT (of this Report)

Approval for public release;

distribution unlimited.

17. DISTRIBUTION STATEMENT (of the abstract entered in Block 20, if different from Report)

18. SUPPLEMENTARY NOTES

DTIC
ELECTE
S DEC 0 6 1982
E

19. KEY WORDS (Continue on reverse side if necessary and identify by block number)

molecular-orbital models, catalysts, alloys

magnetic materials, superconductors

20. ABSTRACT (Continue on reverse side if necessary and identify by block number)

Recent self-consistent-field Xalpha scattered-wave (SCF-Xα-SW) molecular orbital studies of the electronic structures, chemical bonding, and related (e.g. catalytic, magnetic, and superconducting) properties of metal and alloy clusters are reviewed, including results for: (1) Li clusters, (2) Cu, Ni, Pd, and Pt clusters, (3) relativistic contributions to cluster electronic structure, (4) the interaction of hydrogen with

ADA122137

DTIC FILE COPY

Ni, Pd, and Pt clusters, (5) metal-support (Pt-SiO_2^n and Ru-SiO_2^n) interactions, (6) magnetism of Fe clusters, (7) cluster models of transition-metal impurities and their magnetic properties in copper and aluminum hosts, (8) cluster models of intermetallic compounds and solid-solution alloys, (9) cluster models of amorphous alloys, and (10) cluster molecular-orbital models of superconductors.

Accession For	
NTIS GRA&I	☒
DTIC TAB	☐
Unannounced	☐
Justification	
By	
Distribution/	
Availability Codes	
Dist	Avail and/or Special
A	

DTIC
COPY
INSPECTED
2

TECHNICAL REPORT NO. 5

SCF-Xα-SW CLUSTER MOLECULAR-ORBITAL MODELS OF

CATALYSTS, ALLOYS, MAGNETIC MATERIALS, AND SUPERCONDUCTORS

by

K. H. Johnson

Center for Materials Science and Engineering
Massachusetts Institute of Technology
Cambridge, Massachusetts 02139

November 29, 1982

SCF-Xα-SW CLUSTER MOLECULAR-ORBITAL MODELS OF

CATALYSTS, ALLOYS, MAGNETIC MATERIALS, AND SUPERCONDUCTORS

K. H. Johnson
Department of Materials Science and Engineering
Massachusetts Institute of Technology
Cambridge, Massachusetts 02139

ABSTRACT

Recent self-consistent-field Xalpha scattered-wave (SCF-Xα-SW) molecular-orbital studies of the electronic structures, chemical bonding, and related (e.g. catalytic, magnetic, and superconducting) properties of metal and alloy clusters are reviewed, including results for: (1) Li clusters, (2) Cu, Ni, Pd, and Pt clusters, (3) relativistic contributions to cluster electronic structure, (4) the interaction of hydrogen with Ni, Pd, and Pt clusters, (5) metal-support (Pt-SiO_2 and Ru-SiO_2) interactions, (6) magnetism of Fe clusters, (7) cluster models of transition-metal impurties and their magnetic properties in copper and aluminum hosts, (8) cluster models of intermetallic compounds and solid-solution alloys, (9) cluster models of amorphous alloys, and (10) cluster molecular-orbital models of superconductors.

I. INTRODUCTION

The electronic structures and related properties of small transition- and noble-metal clusters are of considerable current interest and importance. For example, the active centers of commercial heterogeneous catalysts often consist of small metallic, bimetallic, or multimetallic clusters, typically based on Group-VIII and IB elements, supported on a refractory material such as silica or alumina.[1-3] The electronic structures of small metallic and bimetallic clusters are also intrinsically interesting to the extent they mimic the bulk metals, and in their utility as models for alloy electronic structure.

In comparison with the large number of band-structure calculations for crystalline metals and alloys,[4] relatively little fundamental work has been directed to the electronic structures of small metallic clusters until recently. Band theory, in its conventional form, is based on the assumptions of long-range crystalline order, Bloch's theorem, and reciprocal- or $\vec{k}$-space representation, which do not apply to small clusters, where there is at most only short-range order.

Molecular-orbital theory, on the other hand, is well suited for describing metal-cluster electronic structure, although applications to transition-metal clusters were originally limited largely to semiempirical molecular-orbital methods.[5] With the development of the self-consistent-field X-alpha scattered-wave (SCF-Xα-SW) approach to molecular-orbital theory,[6] based on the combined use of Slater's Xα density-functional approximation to exchange and correlation[7] and the multiple-scattered-wave method of solving the one-electron Schrödinger equation,[8] it has become practical to calculate the electronic structures of complex polyatomic molecules and clusters from first principles, using only moderate amounts of computer time.[9] The principal objectives of such studies are:

(1) the systematic calculation of the electronic structures of metal and alloy clusters by the SCF-Xα-SW method, with emphasis on clusters containing transition and noble elements;

(2) the use of the calculated electronic structures as a basis for understanding the electronic, magnetic, superconducting, and catalytic properties of small clusters and larger particles including, where necessary, the effects of supporting environments;

(3) the use of the cluster results as a basis for describing local electronic, magnetic, superconducting, and other physical properties of bulk crystalline transition metals and their alloys.

II. APPLICATIONS

A. Li Clusters

Li clusters containing up to 13 atoms were the first metallic aggregates investigated by the SCF-Xα-SW method, including effects of spin polarization.[10] Results of these studies that are of general significance in regard to the physical properties of small metal clusters are: (1) there is a gradual increase of cohesive energy per atom with increasing cluster size and coordination number, a 13-atom cluster yielding approximately 60% of the cohesive energy per atom characteristic of the bulk solid; (2) there is a gradual decrease of first ionization potential (as calculated by the SCF-Xα "transition-state" procedure[6,7]) with increasing cluster size, approaching the bulk work function; (3) a cluster with icosahedral geometry [see Fig. 1(b)] is the most energetically stable of all the clusters considered; (4) where the highest occupied cluster molecular orbital is degenerate, a Jahn-Teller distortion can remove the degeneracy, lower the cluster symmetry, and lower the energy of the cluster.

B. Cu, Ni, Pd, and Pt Clusters

Following the work on Li clusters, SCF-Xα-SW atudies of Cu, Ni, Pd, and
Pt clusters containing up to 13 atoms were carried out and compared with the
results of similar calculations by the extended-Hückel and CNDO methods.
Various phases of this work are presented in Refs. 11-13. One is at first
struck by the systematic similarities, rather than the differences, between
the SCF-Xα electronic structures of the clusters and those of the corresponding
bulk metals. For example, the manifold of orbital energy eigenvalues for 13-
atom clusters having the cubo-octahedral nearest-neighbor coordination [see
Fig. 1(a)] characteristic of the fcc lattice exhibit all the principal features
of the bulk band structures, e.g., overlap of the "d band" by the "s,p band",
a sharp peak in the density of states around the Fermi energy for the Ni_{13},
Pd_{13}, and Pt_{13} clusters, increasing band width through this series, and
magnetic spin polarization in the case of Ni_{13} (see Fig. 2). These results
have more recently been corroborated by SCF-Xα-LCAO calculations on small
nickel clusters,[14] and the inadequacy of symmetry-restricted Hartree-Fock theory
in determining the electronic structures of such clusters has been demonstrated.[15]
The theoretical study of a finite metallic cluster of reasonably high symmetry,
such as the 13-atom cubo-octahedron, has the furhter advantage that, by virtue
of the component molecular-orbital symmetries and charge distributions, its
electronic structure can be partitioned into eigenstates which are delocalized
throughout the cluster (the "bulk-like" states) and eigenstates that are primarily
localized on atoms at the cluster boundary (the "surface-like" states), as shown in
Fig. 3. The electronic structures of such clusters can therefore be used as
analogues of both the bulk and surface electronic structures of the corresponding
crystalline metals, as well as models for small metallic and bimetallic clusters
of catalytic importance.

C. Relativistic Effects

In order to determine the effects of special relativity on the electronic
structures of small transition-metal clusters, we have applied the relativistic

version of the SCF-Xα-SW method, developed by Yang and Rabii,[16] to tetrahedral Ni_4, Pd_4, and Pt_4 clusters, octahedral Ni_6, Pd_6, and Pt_6, and cubo-octahedral Pt_{13} clusters. The relativistic energy-level shifts and spin-orbit splittings are, as anticipated, significant for platinum clusters, relatively small for palladium clusters, and negligible for nickel clusters. The principal relativistic effects on the electronic structure of a platinum cluster are to widen its "d band" and lower its center of gravity on the energy scale in comparison with the nonrelativistic limit. Because SCF-Xα orbital energy eigenvalues, by virtue of their equivalence to derivatives of the total energy with respect to occupation number,[7] can be identified with "orbital electro-negativities,"[17,18] the main effect of relativity is to increase the effective group electronegativity of a platinum aggregate as compared with the nonrela-tivistic limit, thereby affecting its chemisorptive and catalytic properties. For example, the relativistic increase of orbital electronegativity for a platinum aggregate is crucial to explaining why platinum is effectively an electron acceptor, rather than a donor, with respect to atomic hydrogen (see following Section IID). Further details of this work, including a comparison of relativistic and nonrelativistic electronic structures for Pt, Pd, and Ni clusters are published in Ref. 13.

D. Interaction of Hydrogen with Ni, Pd, Pt Clusters

The interaction of atomic hydrogen with small Ni, Pd, and Pt clusters has been studied by the SCF-Xα-SW method, including relativistic effects, as models for hydrogen chemisorption on and interstitial solubility in these transition metals. The nature of the interaction is governed principally by the proximity in energy (or corresponding "orbital electronegativity")[17,18] and concomitant overlap of symmetry-conserving orbitals near the bottom of the cluster d bands with the H 1s orbital. The main result is the splitting off in energy of a hydrogen-metal bonding orbital from the bottom of the d band of each cluster, accompanied by much smaller level shifts within the

d band, as illustrated in Fig. 4 for hydrogen interacting with 4-atom clusters of Ni, Pd, and Pt (relativistic effects included). Because the H 1s orbital (as calculated by the SCF-Xα method) lines up in energy with the nickel cluster spd-hybrid orbital at the bottom of the d band, the relative contributions of Ni atomic orbitals to hydrogen bonding are approximately 60% Ni(4s), 30%Ni(3d), and 10% Ni(4p). In contrast, for palladium and platinum clusters, where the H 1s orbital lines up with the center and top of the respective d bands, the Pd 4d and Pt 5d orbitals account for over 90% of the hydrogen-metal bonding orbital character, thereby dominating the interaction of atomic hydrogen with these metals. The above findings are essentially unaltered for hydrogen interacting with larger Ni, Pd, and Pt clusters. The calculated electronic structures, especially the differences in s- and d-orbital contributions to hydrogen bonding, have been used as a basis for explaining why hydrogen solubility and catalytic activity vary among Ni, Pd, and Pt. Further details are discussed in Ref. 13.

Following the above SCF-Xα-SW studies of atomic hydrogen interacting with Ni, Pd, and Pt clusters, we have investigated the precursor to such interaction, namely, the dissociation of molecular hydrogen (H_2) at low-coordination cluster sites. The previously discussed (see Section IIB and Fig. 3) partitioning of the molecular-orbital eigenstates of a 13-atom cubo-octahedral transition-metal cluster into "bulk" and "surface" components is reproduced schematically in Fig. 5(c). In close analogy to the electronic structure of a coordinatively unsaturated transition-metal complex shown in Fig. 5(a), in which a d_{yz}^* orbital is split off in energy from the nonbonding d orbitals by the strong antibonding interaction with the ligand p-like lone-pair orbitals, the direct interaction of the d orbitals of a metal site on the cluster periphery with the d orbitals on neighboring metal sites (viewed as "ligands") leads to a splitting off in energy of a strongly antibonding d_{yz}^* orbital from the top of the main d-orbital manifold. For cluster geometries other than the one implied in

Fig. 5(c),the most strongly antibonding orbital can have a different local symmetry, e.g., d_{z2}^*, and it is found that for more general cluster configurations or surface morphologies a range of orbital symmetries will be encountered. Such orbitals can be interpreted as cluster analogues of "surface states" that are split off in energy form the top of the d band of a bulk crystalline transition metal. In analogy to the electronic structure of the coordinatively unsaturated transition-metal complex in Fig. 5(a), the d_{yz}^* cluster orbital in Fig. 5(c) is symmetry-conserving with respect to the lowest unoccupied orbitals (σ_u and π^*) of molecules such as H_2 and C_2H_2, thereby facilitating electron flow between the metal cluster and these molecules. This suggests a mechanism for H_2 bond cleavage at a single metal site on the cluster periphery or "surface" analogous to that shown in Fig. 6 for a coordinatively unsaturated metal complex.

E. __Metal-Support ($Pt-SiO_2$ and $Ru-SiO_2$) Interactions__

As prototype models for catalyst-support interactions, we have carried out SCF-Xα-SW molecular-orbital studies of Pt and Ru atoms and aggregates supported on silica (SiO_2). It has already been shown that one can accurately model the electronic structure of pure SiO_2 by performing SCF-Xα-SW molecular-orbital calculations on representative clusters.[19] Although definitive structural data are not yet available,a possible metal-support configuration, consistent with recent EXAFS data,[20] is the one illustrated schematically in Fig. 5(b) in which the oxygen atoms at the SiO_2-M interface serve as "ligands" of the metal atom in a fashion analogous to the coordinatively unsaturated L_2M complex (e.g., L = PH_3: M = Pt) considered in Fig. 5(a).

The primarily covalent interaction between the metal d orbitals and oxygen nonbonding 2p orbitals that constitute the top portion of the SiO_2 valence band lead to metal-oxygen bonding orbitals embedded in the valence band and to nonbonding and antibonding orbitals split off in energy from the top of the valence band and positioned within the SiO_2 band gap. The

highest of these antibonding orbitals is principally metal d_{yz}^* in character
for the chosen coordinate system and has a one-to-one correspondence with the
HOMO of the coordinatively unsaturated L_2M (M = Pt) complex [cf. Fig. 5(a)]
which has been shown in Fig. 6 to be responsible for activation of H_2 dissocia-
tion through symmetry-conserving overlap with the H_2 antibonding σ_u orbital.
These theoretical results suggest that there are strong analogies among
catalytically active sites of (a) molecular transition-metal coordination
complexes, (b) supported metal catalysts, and (c) transition-metal clusters
and particles. The orbital symmetries and orderings are qualitatively similar
for SiO_2Pt and SiO_2Ru, although in the latter system the d_{yz}^* antibonding
orbital is empty. This difference in orbital occupancy suggests that the
bonding and catalytic activity of Ru atoms on silica should be significantly
different from those of Pt atoms on silica. Recent EXAFS, electron microscopy.
and chemisorption studies[20,21] indicate that ruthenium interacts strongly with
a silica substrate, forms "raft-like" structures, and chemisorbs oxygen (O_2)
molecularly, whereas such effects have not yet been observed for Pt supported
on silica. SCF-Xα-SW cluster models for ruthenium aggregates on SiO_2 suggest
that the SiO_2-Ru bonding perpendicular to the silica surface actually enhances
Ru-Ru bonding parallel to the surface, thereby providing a theoretical justifi-
cation for the formation of raft-like structures.

F. Electronic Structure and Magnetic Properties of Fe Clusters

SCF-Xα-SW molecular-orbital calculations have also been carried out for
iron clusters ranging in size from 4 atoms to 15 atoms.[22,23] The calculations
were carried out in spin-unrestricted form, i.e., different orbitals for
different spins, in precisely the same fashion as described for nickel clusters
in Ref. 12. The resulting spin-orbital energy eigenvalues for a 15-atom
cluster having the local coordination up to second-nearest neighbors of bcc
crystalline α-iron are shown in Fig. 7, labeled according to the irreducible
representations of the O_h symmetry group. The two highest occupied spin orbitals,

$6e_g\uparrow$ and $4t_{1u}\downarrow$, are nearly degenerate, partially occupied with one and two electrons, respectively, and determine the cluster Fermi energy (indicated by the dashed line).

From Fig. 7 one can extract the following characteristics which are directly comparable with the band structure of ferromagnetic crystalline α-iron calculated by Tawil and Callaway:[24]

(1) The cluster electronic structure can be characterized in terms of manifolds of predominantly d-like spin orbitals bracketed in energy by orbitals which have significant s,p character, in analogy to the overlap of the d band by the s,p band in bulk crystalline iron.

(2) The Fermi level of the cluster passes through the top of the "spin-up" (↑) d-orbital manifold and through the center of the "spin-down" (↓) d-orbital manifold in a fashion similar to the intersection of the Fermi level with the "majority-spin" and "minority-spin" d bands of ferromagnetic iron (see Fig. 2 of Ref. 24).

(3) The exchange splitting and width of the cluster d band are comparable with the values for bulk ferromagnetic iron.

(4) The cluster total density of states shows a pronounced two-peak structure, which is primarily a consequence of the exchange splitting, consistent with the density of states for ferromagnetic iron (see Fig. 5 of Ref. 24).

(5) The highest occupied and lowest unoccupied cluster "majority-spin" molecular orbitals, $6e_g\uparrow$ and $7t_{2g}\uparrow$, respectively, have <u>antibonding</u> hybrid dsp character, as exemplified by the $7t_{2g}\uparrow$ wavefunction contour map in Fig. 8, plotted in a (110) plane. The solid and dashed contours, respectively, represent positive and negative values of the wavefunction.

The cluster molecular orbitals can be further utilized as a basis for understanding the transition between collective ferromagnetism (or "super-paramagnetism")[25] and local paramagnetism with decreasing particle size or increasing temperature. For example:

(1)   The average paramagnetic magneton numbers per atom for the Fe_9 and Fe_{15} clusters are 2.9 and 2.7, respectively, approaching the 2.2 value for ferromagnetic crystalline α-iron, whereas SCF-Xα results for smaller iron clusters, such as Fe_4, indicate magneton numbers per atom as large as 3.0. The predicted increase of magneton number per atom with decreasing iron cluster size is supported experimentally by Mössbauer studies of small iron aggregates isolated in inert matrices.[26]

(2)   The partial-wave decomposition of the Fe_9 and Fe_{15} cluster spin orbitals indicates that the contribution of the 4s-like components to spin polarization, although relatively small in magnitude, is opposite in direction (antiparallel to) that of the dominant 3d-like components, in good agreement with the analysis of magnetic form factors in polarized neutron scattering data for crystalline iron.[27]

(3)   Somewhat more spin density in the Fe_9 and Fe_{15} clusters is concentrated in the e_g orbitals than in the t_{2g} orbitals, providing a local model for the concentration of spin density along the [100] direction (the direction of easy magnetization) in crystalline α-iron, as deduced from neutron-diffraction measurements.[27,28]

(4)   Neutron-diffraction studies of crystalline iron at temperatures greater than the Curie temperature T_c[29-31] suggest that short-range ordering of spins in the form of "spin clusters" (~ 10Å in size) persists well into the paramagnetic region, and that the paramagnetic magneton number is approximately 25% greater than the value for ferromagnetic iron ($T < T_c$). It is possible, therefore, that the electronic structure of crystalline iron in the paramagnetic region is more appropriately represented statistically by a local spin-polarized cluster model, than by the extended $\vec{k}$-space band-structure description, since the cluster electronic structure is not dependent on the assumption of long-range cyrstalline ordering of spins. Utilizing the bcc Fe_{15} cluster as a prototype model for a "spin cluster," we find that the majority-spin d orbitals, $7t_{2g}\uparrow$ and $6e_g\uparrow$ (see Fig. 7), are the highest partially occupied and lowest unoccupied orbitals near

the Fermi energy at T = 0°K. Thermally induced "spin-flip" electronic excitations from the highest occupied orbitals of the minority-spin d manifold to the unoccupied $7t_{2g}\uparrow$ and $6e_g\uparrow$ orbitals for $T > T_c$ results in an effective 30% increase of cluster magnetic moment and magneton number, thereby providing a good model for the observed 25% increase in magnetic moment of crystalline iron in the paramagnetic region. Such excitations only slightly alter the average exchange splitting and total density of states of the cluster, consistent with the apparent persistence of the local density of states for crystalline iron at $T > T_c$ (as measured, for example, by photoemission), an experimental observation which heretofore has been inexplicable within the framework of conventional ferromagnetic energy-band theory.

G. Cluster Molecular-Orbital Model for the Local Electronic Structure,
Chemical Bonding, and Magnetic Moments of Transition-Metal Impurities
in Copper

Spin-unrestricted self-consistent-field X-alpha scattered-wave (SCF-Xα-SW) cluster molecular-orbital models have been constructed for transition-metal impurities (Ni, Fe, Mn, and V) alloyed in crystalline copper, in order to gain insight into the occurrence of local magnetic mements and the Kondo effect,[32,33] traditionally viewed as many-body effects arising from the interaction of the transition-metal impurities with the conduction electrons of the host metal. A 19-atom cluster representing the local molecular environment (12 nearest neighbors and 6 second-nearest neighbors) of an isolated transition-metal impurity in an otherwise perfect crystalline copper lattice yields manifolds of molecular-orbital energy levels (such as those shown in Fig. 9 for iron in copper) corresponding to the copper "d band", bracketed by impurity d-orbital energy levels of e_g and t_{2g} symmetries that are bonding with respect to the bottom of the copper d band and antibonding with respect to the top of the d band. The antibonding cluster orbitals (see inset of Fig. 9) in conjunction with Hund's rules, (1) are discrete analogues of Friedel-Anderson[34,35] virtual im-

purity states, (2) satisfy a "sum rule" analogous to the Friedel sum rule, (3)

have spin occupancies and polarization in accord with measured magnetic moments,

(4) are consistent with measured trends of residual electrical resistivity, and

(5) describe the "renormalizing" effects of the local crystalline environment on

the transition-metal impurity atom. The distribution of occupied $FeCu_{12}Cu_6$ cluster

spin-orbital energy levels is in good agreement with the X-ray photoelectron

spectrum (XPS) recently measured by Höchst et al.[36] for a dilute alloy of iron

in copper, as shown in Fig. 9 (Fermi level indicated by the dashed line).[†] In

particular, the broad "shoulder" in the XPS spectrum between the Cu d-band

maximum and the Fermi energy, is explained in the present theoretical model as

arising from the e_g and t_{2g} molecular orbitals above the Cu d band which have

significant Fe 3d σ^* and π^* antibonding components (the Fe 3d percentages are

indicated in parentheses in Fig. 9). The most striking result of these theoretical

studies is the discovery that local coordination chemical bonding dominates the

interaction of the transition-metal impurity with its crystalline environment,

yielding a large splitting ($\sim$ 4-4.5 eV) between bonding and antibonding impurity

molecular-orbital energy levels (see Fig. 9) and a spin splitting ($\sim$ 0.2-0.6 eV)

of the highest occupied antibonding t_{2g} and e_g orbitals (the Friedel-Anderson-

like impurity states) that is an order of magnitude smaller than values assumed

in previous theoretical models (e.g., the Anderson[35] model).[†] The near

degeneracy of the latter t_{2g} and e_g spin orbitals (for Fe and Mn impurities) with

cluster a_{1g} molecular-orbital analogues of the sd conduction-band eigenstates

of crystalline copper near the Fermi energy (see inset of Fig. 9) suggests that

the "spin-compensation cloud" often associated with the Kondo effect is consider-

ably smaller in magnetization and more spatially localized around the impurity

than assumed in previous formal theories[33] and, in conjunction with the SCF-Xα

[†]A recently published density-functional model for magnetic impurities in copper
by Podloucky et al. [Phys. Rev. B22, 5777 (1980)], which does not properly include
the chemical bonding effects of the local crystalline environment on the im-
purity site is in qualitative disagreement with the present theoretical model and
with the XPS measurements of Höchst et al.[36] and merely reproduces the Anderson model.

transition-state concept, also provides a discrete orbital basis for discussing the onset of "localized spin fluctuations" around the Kondo temperature. The possible contributions of spin-orbit coupling and Jahn-teller effects to impurity electronic structure have been determined, with detailed examples of how the former effect can lead to the quenching of the impurity magnetic moment below the Kondo temperature. Further details of this work are presented in Ref. 37.

H. Cluster Molecular-Orbital Model for the Local Electronic Structure, Chemical Bonding, and Magnetic Moments of Transition-Metal Impurities in Aluminum

SCF-Xα-SW cluster molecular-orbital studies of the type described in the preceding Section G have been extended to the problem of transition-metal impurities in aluminum. First-row transition-metal (Ti, V, Cr, Mn, Fe, Co, and Ni) atoms were successively substituted for the central Al atom in a cluster representing the local environment of bulk fcc crystalline aluminum, in a fashion similar to that described in Section G for a copper host, except that in the present case a 43-atom cluster ($AlAl_{12}Al_6Al_{24}$) representing the aluminum host up to third nearest neighbors was chosen to model the somewhat more delocalized electronic structure of this material. Indeed, previous SCF-Xα-SW studies of a 43-atom aluminum cluster by Salahub and Messmer[38] have demonstrated that this cluster yields a manifold of s,p σ- and π-bonding molecular orbitals having a total band width and general character consistent with the band structure of crystalline aluminum, as shown in Fig. 10, and in good agreement with measured XPS data for crystalline aluminum, as shown in Fig. 11.

Perhaps the most striking feature of the SCF-Xα-SW results for the 43-atom pure aluminum cluster is the π-bonding character of the highest occupied molecular orbital ($8t_{1u}$ in Fig. 10), i.e., the molecular orbital that coincides with the Fermi level, the wavefunction contour map of which is

shown in Fig. 12, plotted in a (200) plane up to second-nearest-neighbor atoms. As will be shown in Section IIK, the spatially extended π-bonding topology of this orbital is a precursor to superconductivity in pure aluminum. This "real-space" character of aluminum molecular orbitals at the Fermi energy cannot be extracted easily from the conventional "reciprocal ($\vec{k}$)-space" Bloch description of the crystal band structure (see Fig. 10), except in hindsight as an appropriate combination of Σ_1, Σ_3, and Δ_1 Bloch eigenstates, and thus has eluded solid-state physics.

The SCF-Xα-SW molecular-orbital energy levels for a Mn impurity substituted for the central atom of the 43-atom aluminum cluster are shown in Fig. 13, where they are compared with the 3d energy level of an isolated free Mn atom (and with the 3d atomic energy levels of the other first-row transition elements). The cluster results are also compared directly with XPS data for a dilute AlMn alloy recently obtained by Steiner et al.[39] Comparison of Fig. 13 with the results for pure aluminum in Fig. 11 reveals that the main effects of alloying Mn impurities in an aluminum host, neglecting impurity-impurity interactions, are: (1) to empty out locally the otherwise spatially extended t_{1u} pπ-bonding orbital mapped in Fig. 12, and (2) for the Mn 3d orbitals to overlap and hybridize with the surrounding Al 3p orbitals to produce a narrow manifold of occupied spatially localized bonding and antibonding t_{2g} and e_g molecular orbitals near the Fermi energy (indicated by the dashed line in Fig. 13), which are responsible for the peak in XPS intensity just below the Fermi energy. The t_{2g} and e_g bonding and antibonding orbitals containing 38% or more Mn 3d character (indicated in parentheses in Fig. 13) are mapped in Figs. 14 through 17. The highest occupied molecular orbitals are nearly degenerate t_{2g} and e_g dpσ*-dpπ* antibonding orbitals, as indicated in the inset of Fig. 13 (cf. inset of Fig. 11). The dpσ*-dpπ* antibonding topology is clearly evident in the wavefunction contour maps of Figs. 16 and 17. These molecular orbitals are analogous to the t_{2g} and e_g dsdσ*-ddsπ* antibonding

orbitals shown in the inset of Fig. 9 and in Section G to be associated with the local spin magnetic moment of an Fe impurity in a copper host above the Kondo temperature. However, for Mn impurities in aluminum, the fluctuations in occupancy of the nearly degenerate t_{2g} and e_g antibonding orbitals at the Fermi energy by five electrons (see inset of Fig. 13), coupled with a relatively small exchange splitting of the orbital energies, prevent stable magnetic moment formation and are responsible for "spin fluctuations" in the AlMn system.[33] These antibonding orbitals also provide a straightforward explanation of the destructive effect of the Mn impurities on the superconductivity of aluminum in terms of the emptying out of the t_{1u} ($p\pi$) orbital.

SCF-Xα-SW cluster molecular-orbital models for Fe, Co, and Ni impurities in aluminum show a systematic downward shift in energies and full electron occupancy of the bonding and antibonding impurity-derived orbitals with respect to the Fermi energy. This trend is consistent with the relative energies of the corresponding atomic 3d orbitals in Fig. 13, explains the nonmagnetic ground states of these impurities in aluminum,[33] is in good agreement with the positions of the peaks in XPS intensity for these alloys,[39] and suggests that the effective cancellation of occupied bonding orbitals by occupied antibonding orbitals is largely responsible for the very low solubility of these impurities in aluminum.

Further details of the above results will appear in a later publication.[40]

I.   Local Electronic Structures and Chemical Bonding of Intermetallic
     Compounds and Solid-Solution Alloys

The SCF-Xα-SW cluster molecular-orbital method has been used to determine the local electronic structures of the intermetallic compound Ni_3Ti and solid-solution alloy $\alpha CuZn$. It has been found that relatively small clusters which preserve local compositional and structural order yield local densities of states comparable to those obtained in more elaborate band-structure theories, provide a realistic model for local chemical bonding effects neglected in

traditional $\vec{k}$-space alloy theories, and lead to a "real-space" chemical description of alloy phase stability. For the example of Ni_3Ti, the cluster electronic structure provides a simple yet remarkably accurate interpretation of photoemission spectra for this compound recently measured by Fischer and Kelemen. Details are published in Ref. 41.

J.   Local Electronic Structure and Chemical Bonding of Amorphous Alloys

A unified conceptual basis for understanding and predicting the electronic structures and glass-forming capabilities of amorphous alloys has been developed, using the results of first-principles self-consistent-field X-alpha (SCF-Xα-SW) cluster molecular-orbital calculations. Prototype cluster models have been constructed for Cu-Zr, Ni-Ti, and Pd-Si alloys which exemplify two major classes of binary (A-B) glass-forming systems, namely:

(1) Metallic glasses based on noble or transition elements (e.g., A = Cu, Ni) toward the right of the periodic table and transition elements (e.g., B = Zr, Ti) toward the left of the periodic table.

(2) Metalloid glasses based on transition elements (e.g., A = Pd) toward the right of the periodic table and nonmetallic elements (e.g., B = Si) toward the middle of the periodic table.

The calculated electronic structures are in excellent quantitative agreement with and provide an interpretation of published photoelectron spectra for the above amorphous alloys. All three systems investigated are characterized by a fully occupied d-band associated principally with the A (e.g., Cu, Ni, Pd) components and a partially occupied band lying at somewhat higher energies and associated mainly with the B (e.g., Zr, Ti, Si) components, although there is significant A-B bonding and B-A antibonding character within these respective bands and some electron transfer from B to A.

The most striking feature of the calculated electronic structures is the nature of the electronic states coinciding with or just below the Fermi energy, i.e., the highest occupied molecular orbitals. These states can be described

as forming highly delocalized and spatially directed B-B (e.g., Zr-Zr d-orbital or Si-Si p-orbital) chemical bonds which are promoted, in part, by the composite bonding-antibonding interaction with the d-orbitals localized on neighboring A (e.g., Cu or Pd) components. These bonds are clearly visible in the molecular-orbital wavefunction contour maps shown in Fig. 18 for the Cu-Zr and Pd-Si systems, respectively, where the solid and dashed contours represent positive and negative phases of the wavefunction, respectively.

The existence of directed Zr-Zr and Si-Si bonds in amorphous Cu-Zr and Pd-Si alloys, respectively, may, at first sight, seem surprising since the Zr and Si atoms are not nearest neighbors in these alloys, and the Zr-Zr and Si-Si bond distances are significantly larger than those in elemental solid Zr and Si. Nevertheless, the effects of the nearest-neighbor Cu and Pd d-orbitals in acting as "bridges" for the formation of Zr-Zr and Si-Si bonds are clearly evident in the above contour maps.

On a scale spanning many atoms, the Zr-Zr and Si-Si bonds form a type of spatially extended "electron network" or "electron superlattice" in the vicinity of the Fermi energy, which we believe is related to the glass-forming capabilities of these and similar alloys. In the case of the Cu-Zr system, the electron network orbital topology at the Fermi energy is precisely of the type recently found by this author (see the following Section K) to be necessary for the occurrence of superconductivity in a material. Indeed, amorphous Cu-Zr alloys have recently been observed to be superconducting.[42]

K. Molecular Orbitals and Superconductivity

A real-space molecular-orbital description of electronic wavefunctions which are postulated to be the precursors of the superconducting state in metals, alloys, compounds, amorphous, and organic solids is presented, based on self-consistent-field X-alpha scattered-wave (SCF-Xα-SW) molecular-orbital calculations for clusters representing the local molecular environments in these materials. It is shown that there is a persistent correlation between the

occurence of superconductivity in a material and the existence of spatially

delocalized molecular orbitals at the Fermi energy which are bonding within

and antibonding between "layers" or "tubes" of overlapping atomic orbitals

that span many atoms, forming a type of "electron superlattice" or "network"

at the Fermi energy, as exemplified by $p\pi$ "layered" molecular-orbital components

ψ_+ and ψ_- in Al and $(TMTSF)_2PF_6$ (see Fig. 19, the three-dimensional version of

Fig. 12), and by $d\delta$ "tubular" molecular-orbital components ψ_+ and ψ_- in Nb

and Nb_3Sn (see Figs. 20 and 21, respectively). This description of the precursor

superconducting state is consistent with the original conjectures of London[43] that

the superconducting-state wavefunction is "molecular" in nature, "rigid" in

character, and of wide spatial extent, form which observed physical properties

(e.g., diamagnetism and nondissipative electrical currents) of the superconducting

state logically follow. The molecular-orbital model is further shown to be

consistent with Cooper's concept of electron pairing in the superconducting state

through a net attractive electron-electron interaction but differs from the

Bardeen-Cooper-Schrieffer (BCS)[44] theory of superconductivity in attributing

the pairing to "valence-bond-like" electron occupation of layered or tubular

molecular orbitals at the Fermi energy, rather than to the absorption and

emission of virtual phonons. However, recent simple physical arguments presented

by Weisskopf[45] for the formation of Cooper pairs suggest that the two points

of view are not incompatible. Approximate formulae for calculating the electron

pair binding energy and superconducting transition temperature, analogous

to the BCS formulae but expressed entirely in terms of two simple molecular-orbital

parameters, have been derived and applied to various superconductors. Moreover,

through an elementary phase-space argument, the molecular-orbital description of

Cooper pairs is shown to be qualitatively consistent with Schafroth's[46] description

of electron pairs as "quasi-molecules" undergoing Bose-Einstein-like condensation

to the superconducting state. The above molecular-orbital criteria for super-

conductivity are diametrical to those for the occurrence of local magnetic

moments and ferromagnetism, namely, the existence of spatially localized,

exclusively <u>antibonding</u> (e.g., $d\sigma^*$, $d\pi^*$, or $d\delta^*$) molecular orbitals near the Fermi energy. Furthermore, in contrast to the ordering of electron spins on atomic sublattices in conventional antiferromagnetism, the valence-bond-like correlation of Cooper-Schafroth electron pairs at the Fermi energy in composite bonding-antibonding layered or tubular molecular-orbital components, spatially delocalized between the atoms, corresponds to a type of conduction-electron "antiferromagnetism" or spin density wave, thus offering an explantion for the occurrence of this antiferromagnetism in superconductors such as $(TMTSF)_2PF_6$[47] and Nb_3Sn.[48] These molecular-orbital criteria therefore provide a conceptual basis for understanding the generally mutually exclusive incidence of super-conductivity and magnetism among the elements of the periodic table, although they can also be used to explain the occasional coexistence of superconductivity and ferromagnetism or antiferromagnetism in some materials. The molecular-orbital model for superconductivity complements BCS theory in that it permits the prediction of which materials are likely to be superconductors and which are not entirely on the basis of the molecular-orbital topology at the Fermi energy. It offers an explanation of the vanishing isotope effect in certain superconductors. It contributes to the clarification of the issue of non-phonon mechanisms of superconductivity. It provides insight into the correlations of superconductivity with other physical properties, such as lattice instabilities. It is readily applicable to superconductors lacking long-range crystalline order, such as amorphous alloys and small particles. Finally, the molecular-orbital approach can be used to explain in simple terms why some materials (e.g., Cu, Ag, and Au) are neither superconducting nor magnetic, why certain quasi-one-dimensional organic solids, such as TTF-TCNQ, are not superconductors while others, such as $(TMTSF)_2PF_6$, are superconductors,[47] and to assess critically the likelihood of superconductivity in certain other types of substances (e.g., other types of organic solids; metallic hydrogen at attainable high pressures), and to suggest ways of systematically improving existing classes or synthesizing novel classes of superconducting materials. Further details will appear in other publications.[49]

-20-

III. ACKNOWLEDGMENTS

REFERENCES

1. M. Boudart, in Proceedings of the Robert A. Welch Foundation Conference on Chemical Research. XIV Solid State Chemistry, edited by W.O. Milligan (The Robert A. Welch Foundation, Houston, Texas, 1970), p. 299.

2. J.H. Sinfelt, in Annual Review of Materials Science, edited by R.A. Huggins, R.H. Bube, and R.W. Roberts (Annual Reviews, Palo Alto, California, 1972), V. 2, p. 641.

3. J.F. Anderson, Structure of Metallic Catalysts (Academic, New York, 1975).

4. Electronic Density of States, edited by L.H. Bennett (National Bureau of Standards Spec. Pub. 323, Washington, D.C. 1971).

5. R.C. Baetzold, J. Chem. Phys. 55, 4363 (1971); J. Catal. 29, 129 (1974); R.C. Baetzold and R.E. Mack, J. Chem. Phys. 62, 1513 (1975); A.B. Anderson and R. Hoffman, J. Chem. Phys. 61, 4545 (1974); G. Blyholder, J. Chem. Phys. 62, 3193 (1975).

6. J.C. Slater and K.H. Johnson, Phys. Rev. B5, 844 (1972); K.H. Johnson and F.C. Smith, Jr., Phys. Rev. B5, 831 (1972); J.C. Slater and K.H. Johnson, Physics Today 27, 34 (1974).

7. J.C. Slater, in Advances in Quantum Chemistry, Vol. 6, edited by P.-O. Löwdin (Academic, New York, 1972), p. 1; J.C. Slater, The Self Consistent Field for Molecules and Solids, Vol. 4 of Quantum Theory of Molecules and Solids (McGraw-Hill, New York, 1974)

8. K.H. Johnson, J. Chem. Phys. 45, 3085 (1966); K.H. Johnson, in Advances In Quantum Chemistry, Vol. 7, edited by P.-O.Löwdin (Academic, New York, 1973), p. 143.

9.   K.H. Johnson, in Annual Review of Physical Chemistry, Vol. 26, edited by
      H. Eyring, C.J. Christensen, and H.S. Johnston (Annual Reviews, Palo Alto,
      California, 1975), p. 39.

10.   J.G. Fripiat, K.T. Chow, M.Boudart, J.B. Diamond, and K.H. Johnson,
      J. Molec. Catal. 1, 59 (1975); C.Y. Yang and K.H. Johnson (unpublished
      work).

11.   R.P. Messmer, C.W. Tucker,Jr., and K.H. Johnson, Chem. Phys. Lett. 36,
      423 (1975).

12.   R.P. Messmer, S.K. Knudson, K.H. Johnson, J.B. Diamond, and C.Y. Yang,
      Phys. Rev. B13, 1396 (1976).

13.   R.P. Messmer, D.R. Salahub, K.H. Johnson, and C.Y. Yang, Chem. Phys.
      Lett. 51, 84 (1977).

14.   R.P. Messmer and S.H. Lamson, Chem. Phys. Lett. (in press).

15.   R.P. Messmer, C.M. Kao, and T.C. Caves, Chem. Phys. Lett (in press).

16.   C.Y. Yang and S. Rabii, Phys. Rev. A12, 362 (1975); C.Y. Yang, Chem.
      Phys. Lett. 41, 588 (1976).

17.   K.H. Johnson, Intern. J. Quantum Chem. 11S, 39 (1977).

18.   K.H. Johnson, Crit. Rev. Solid State and Mat. Sci. 7, 101 (1978).

19.   J.A. Tossell, D.J. Vaughan, and K.H. Johnson, Chem. Phys. Lett. 20, 329
      (1973); J.A. Tossell, J. Am. Chem. Soc. 97, 4840 (1975); J. Phys. Chem.
      Solids 36, 1723 (1975).

20.   F.W. Lytle, G.H. Via, and J.H. Sinfelt, J. Chem. Phys. 67, 3831 (1977).

21.   E.B. Prestidge, G.H. Via, and J.H. Sinfelt, J. Catal. 50, 115 (1977).

22.   C.Y. Yang, Ph.D. Thesis, Department of Materials Science and Engineering,
      Massachusetts Institute of Technology, June, 1977.

23.   C.Y. Yang, K.H. Johnson, D.R. Salahub, J. Kasper, and R.P. Messmer,
      Phys. Rev. B24, 5673 (1981).

24.   R.A. Tawil and J. Callaway, Phys. Rev. B7, 4242 (1973).

25.   B. Abeles, in Applied Solid State Science (Academic, New York, 1976),
      P. 90.

26. P.A. Montano, P.H. Barrett, and Z. Stanfield, Solid State Comm. 15, 1675 (1974); J. Chem. Phys. 64, 2896 (1976).

27. C.G. Shull and Y. Yamada, J. Phys. Soc. Japan 17S, BIII, 1 (1962).

28. C.G. Shull and H.A. Mook, Phys. Rev. Lett. 16, 184 (1966).

29. M.K. Wilkinson and C.G. Shull, Phys. Rev. 103, 516 (1956).

30. H.A. Gersch, C.G. Shull, and M.K. Wilkinson, Phys. Rev. 103, 103 (1956).

31. S. Spooner and B.L. Averbach, Phys. Rev. 142, 291 (1966).

32. A.J. Heeger, in Solid State Physics, edited by F. Seitz, D. Turnbull, and H. Ehrenreich (Academic, New York, 1969), Vol. 23, p. 283.

33. G. Grüner, Adv. in Phys. 23, 941 (1974).

34. J. Friedel, Can. J. Phys. 34, 1190 (1956); J. Phys. Radium 19, 573 (1958); Suppl. Nuovo Cimento VII, 287 (1958).

35. P.W. Anderson, Phys. Rev. 124, 41 (1961).

36. H. Höchst, P. Steiner, and S. Hüfner, Z. Phys. B38, 201 (1980).

37. K.H. Johnson, D.D. Vvedensky, and R.P. Messmer, Phys. Rev. B19, 1519 (1979).

38. D.R. Salahub and R.P. Messmer, Phys. Rev. B16, 2526 (1977).

39. P. Steiner, H. Höchst, W. Steffen, and S. Hüfner, Z. Phys. B38, 191 (1980).

40. K.H. Johnson, Phys. Rev. (manuscript in preparation).

41. T.E. Fischer, S.R. Kelemen, K.P. Wang, and K.H. Johnson, Phys. Rev. B20, 3124 (1979).

42. O. Rapp, B. Lindberg, H.S. Chen, and K.V. Rao, J. Less-Common Metals 62, 221 (1978).

43. F. London, Superfluids, Vol. 1 (Wiley, New York, 1950).

44. J. Barden, L.N. Cooper, and J.F. Schrieffer, Phys. Rev. 108, 1175 (1957); L.N. Cooper, Phys. Rev. 104, 1189 (1956).

45. V.F. Weisskopf (to be published and private communication).

46. M.R. Schafroth, J.M. Blatt, and S.T. Buther, Helv. Phys. Acta 30, 93 (1957); M.R. Schafroth, Phys. Rev. 130, 1244 (1958).

-23-

47. Physics Today $\underline{34}$, 17 (1981).

48. S.N. Ekbote and A.V. Narlikar, Mat. Res. Bull. $\underline{15}$, 827 (1980).

49. K.H. Johnson and R.P. Messmer, Synth. Metals (in press).

FIGURE CAPTIONS

Fig. 1   Cubo-octahedral cluster containing 13 atoms.

Fig. 2   Spin-polarized SCF-Xα-SW electronic energy levels for a cubo-
octahedral Ni_{13} cluster with near-crystalline nickel. Levels
are labeled according to the irreducible representations of
the O_h symmetry group. "Fermi level" E_F separates the
occupied levels from the unoccupied ones.

Fig. 3   Separation of the SCF-Xα-SW electronic energy levels for Cu_{13}
and Ni_{13} clusters into "bulk" and "surface" components.

Fig. 4   SCF-Xα orbital energies of tetrahedral group-VIII transition-
metal clusters with and without interstitial atomic hydrogen,
including relativistic corrections for the Pd_4, Pd_4H, Pt_4,
and Pt_4H clusters.

Fig. 5   Comparison of the electronic structures associated with
coordinatively-unsaturated transition-metal (e.g., M = Pt)
sites: (a) in a transition-metal coordination complex
(L = PH_3); (b) on a silica (SiO_2) support; (c) at the
periphery or "surface" of a transition-metal cluster.
Also shown, for comparison, are the HOMO and LUMO of
the reactant molecules; (d) H_2 and (e) C_2H_2. All the
orbital energy levels shown in the lower half of the
diagram are displayed schematically on the same relative
scale and for M = Pt in (a), (b) and (c) span an energy
range of approximately 0.5 Ry. Symmetry-conserving
orbital wavefunctions involved in reactivity are mapped
in the y-z plane in the upper half of the diagram.

Fig. 6   Proposed orbital mechanism for H_2 dissociation at a
coordinatively-unsaturated transition-metal site.

Fig. 7   Orbital eigenvalues from the spin-polarized calculation for Fe_{15}.
The dashed line indicates the position of the Fermi level, which
is coincident with the $6e_g^{\uparrow}$ (one electron) and $4t_{1g}^{\downarrow}$ (two electrons)
levels. The bottom line shows the number of electrons of each
spin and symmetry type (point group O_h) as well as the total
number of majority- and minority-spin electrons.

Fig. 8   Contour map of the lowest unoccupied "majority-spin" molecular
orbital, $7t_{2g} \uparrow$ (see Fig. 7), of an Fe_{15} cluster. The solid
and dashed contours represent positive and negative values,
respectively, of the wave function.

Fig. 9   SCF-Xα-SW spin-polarized molecular-orbital energy levels of
19-atom cluster representing the local environment of an Fe
impurity in a copper crystal up to second-nearest neighbors.
The calculated levels are compared with the measured X-ray
photoelectric spectrum (XPS) of bulk copper containing a
dilute concentration of substituional Fe impurities.

Fig. 10   Comparison of the SCF-Xα-SW molecular-orbital energy levels
of a 43-atom aluminum cluster, representing the local
environment of fcc crystalline aluminum up to third-nearest
neighbors, with the bulk energy bands.

Fig. 11   Comparison of the SCF-Xα-SW molecular-orbital energy levels
of a 43-atom aluminum cluster, representing the local
environment of crystalline aluminum up to third-nearest
neighbors, with the measured X-ray photoelectron spectrum
(XPS) of an aluminum crystal.

Fig. 12   Contour map of the wave function for the highest occupied
molecular orbital, $t_{1u}(\varepsilon_F)$, of a 43-atom aluminum cluster,
plotted in the (200) crystallographic plane up to second-
nearest neighbors. The solid and dashed contours represent
positive and negative values, respectively, of the wave
function.

Fig. 13   SCF-Xα-SW molecular-orbital energy levels of a 43-atom
           cluster representing the local environment of a Mn
           impurity of an aluminum crystal up to third-nearest
           neighbors. The calculated levels are compared with
           the measured X-ray photoelectron spectrum (XPS) of
           bulk aluminum containing a dilute concentration of
           substitutional Mn impurities.

Fig. 14   Contour map of the highest occupied bonding t_{2g} cluster
           molecular-orbital wavefunction for a Mn impurity in an
           aluminum crystal.

Fig. 15   Contour map of the highest occupied bonding e_g cluster
           molecular-orbital wavefunction for a Mn impurity in an
           aluminum crystal.

Fig. 16   Contour map of the highest occupied antibonding t_{2g}
           cluster molecular-orbital wavefunction for a Mn
           impurity in an aluminum crystal.

Fig. 17   Contour map of the highest occupied antibonding e_g
           cluster molecular-orbital wavefunction for a Mn
           impurity in an aluminum crystal.

Fig. 18   (a) Contour map of the wave function for the cluster
                molecular orbital at the Fermi energy of amorphous
                Cu-Zr.

           (b) Contour map of the wave function for the cluster
                molecular orbital at the Fermi energy of amorphous
                Pd-Si.

Fig. 19   Three-dimensional contour map of the wavefunction for
           the highest occupied molecular orbital, $t_{1u}(\epsilon_F)$, of
           a 43-atom aluminum cluster.
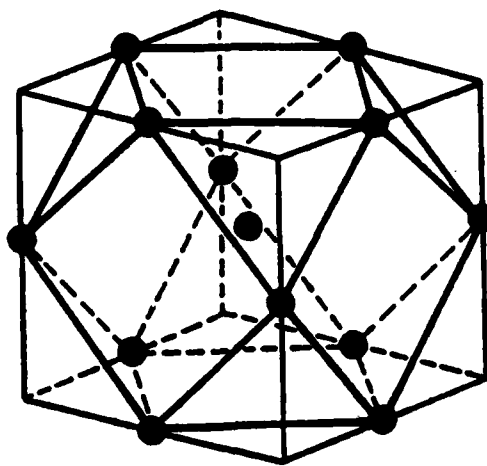
(a)
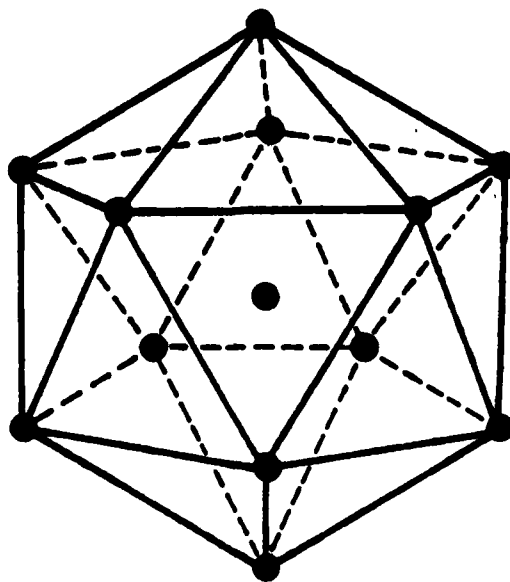
(b)

FIGURE 1

FIGURE 2

FIGURE 3

FIGURE 4

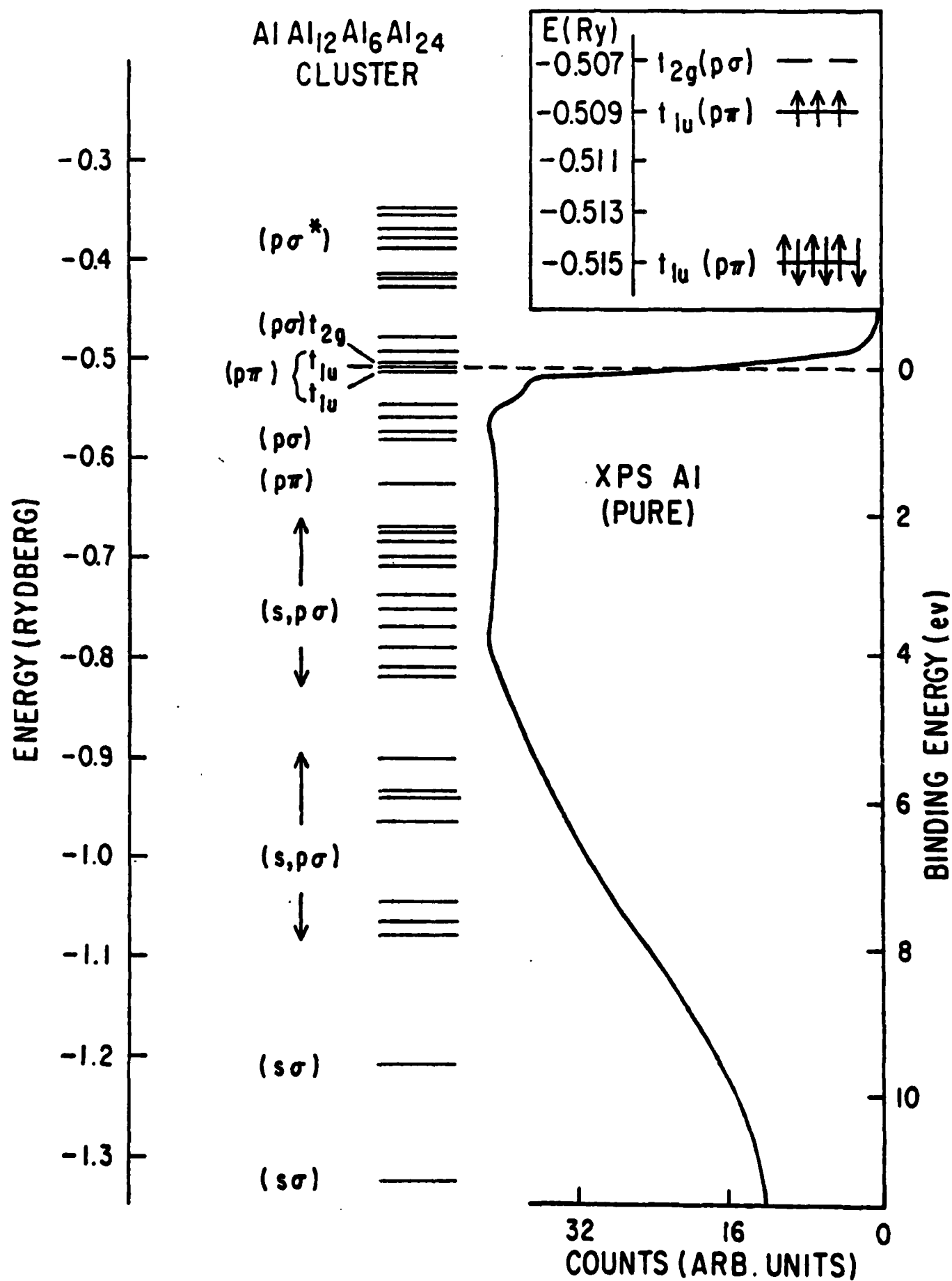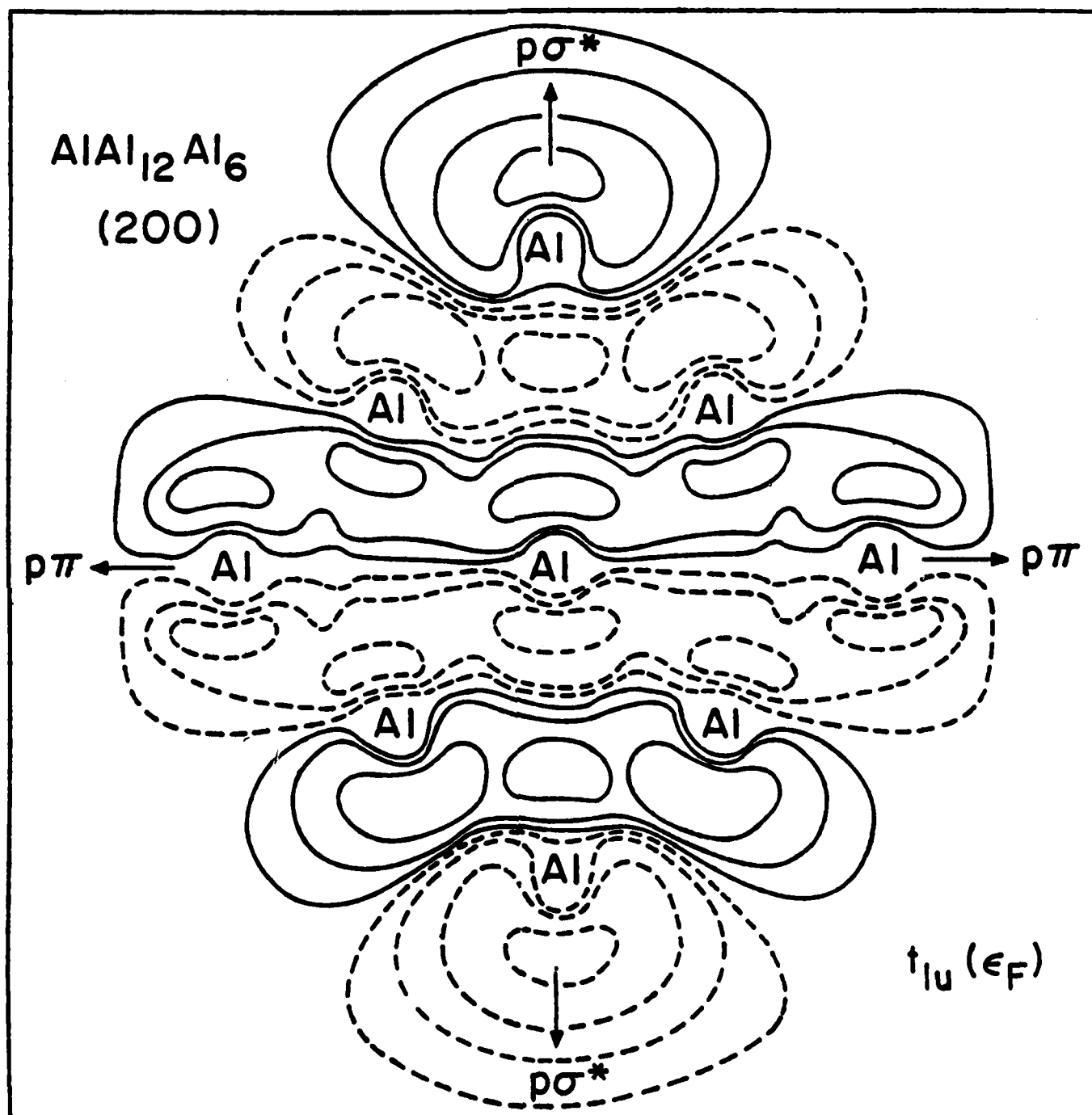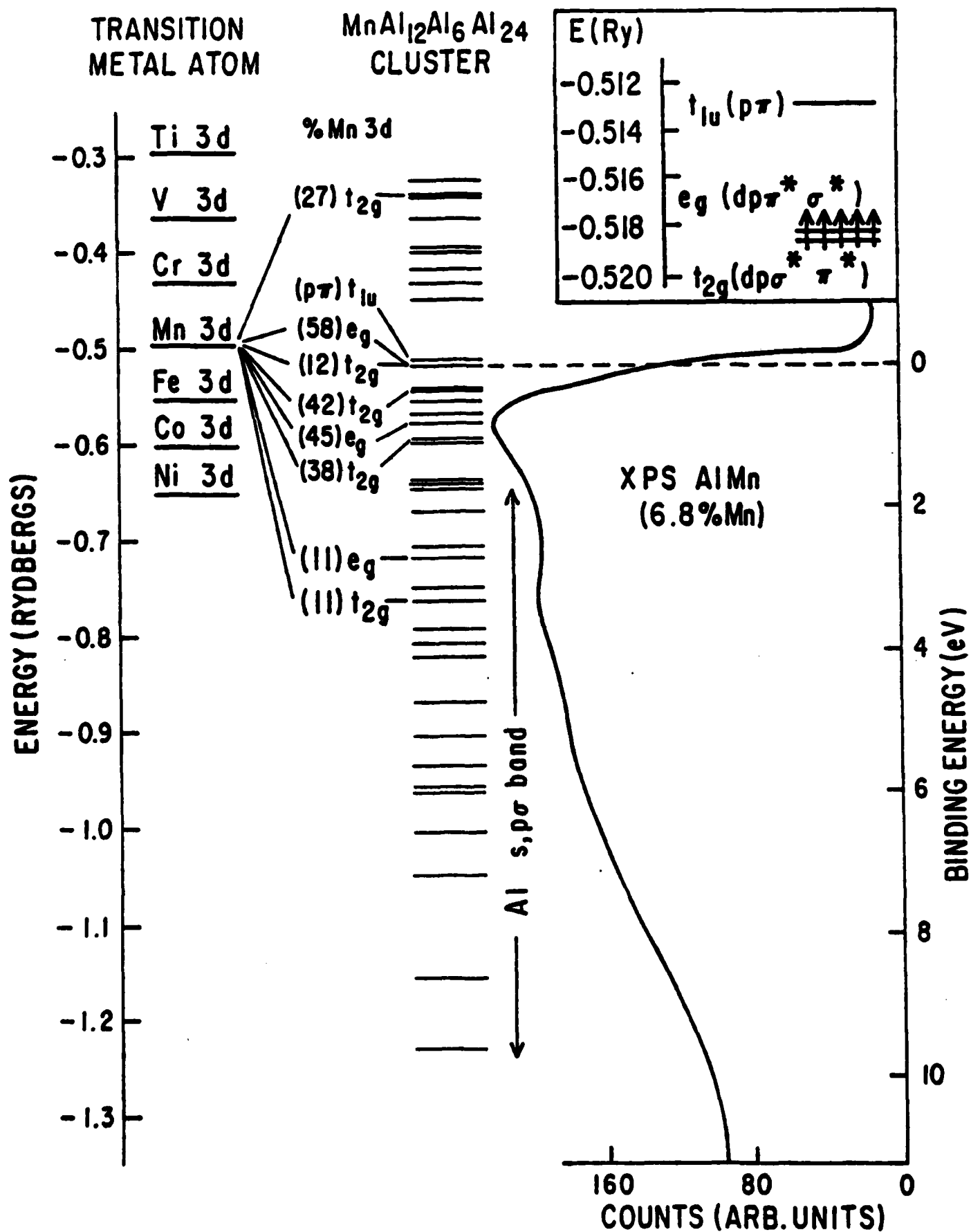FIGURE 5

FIGURE 6

-34-
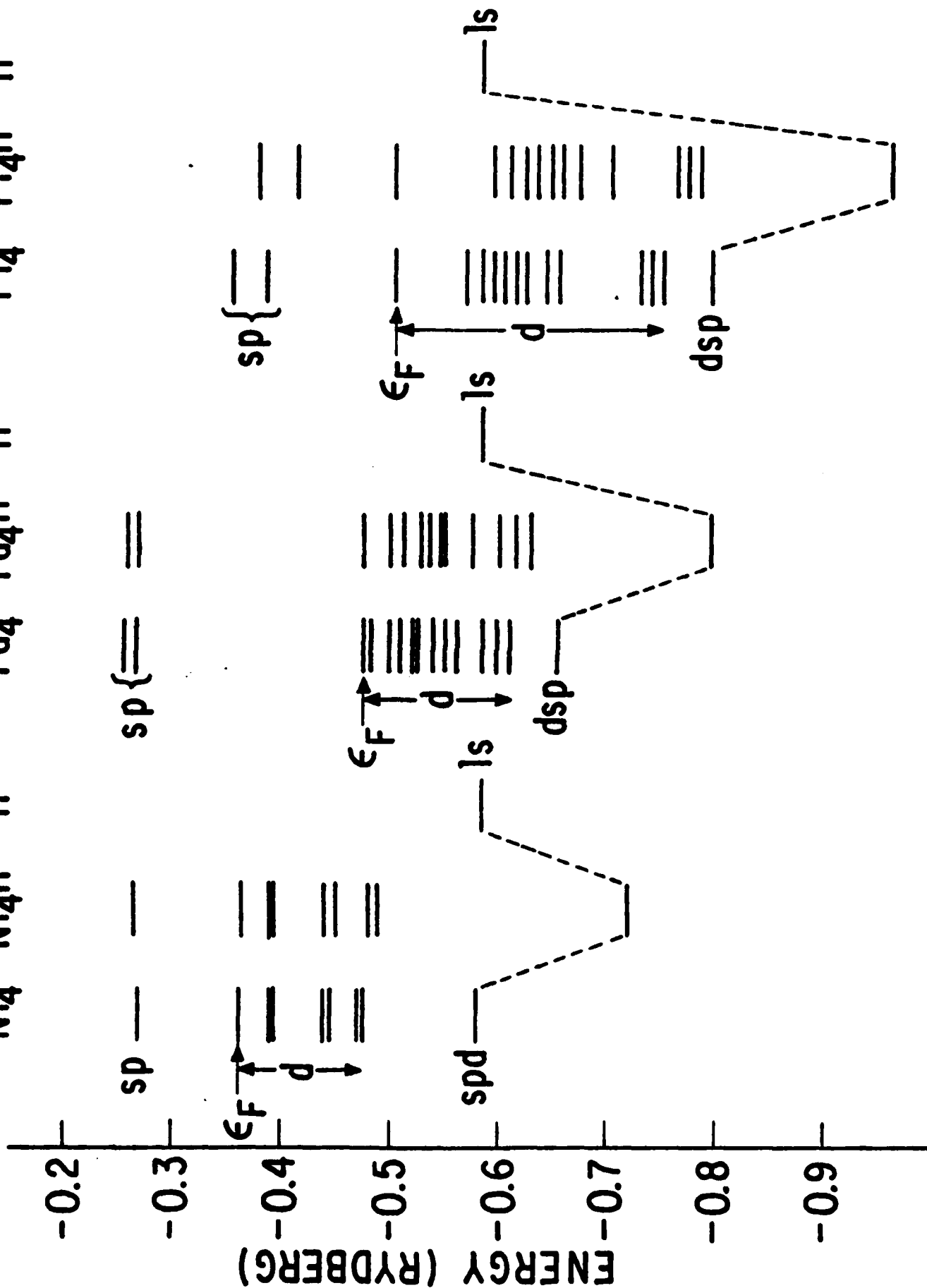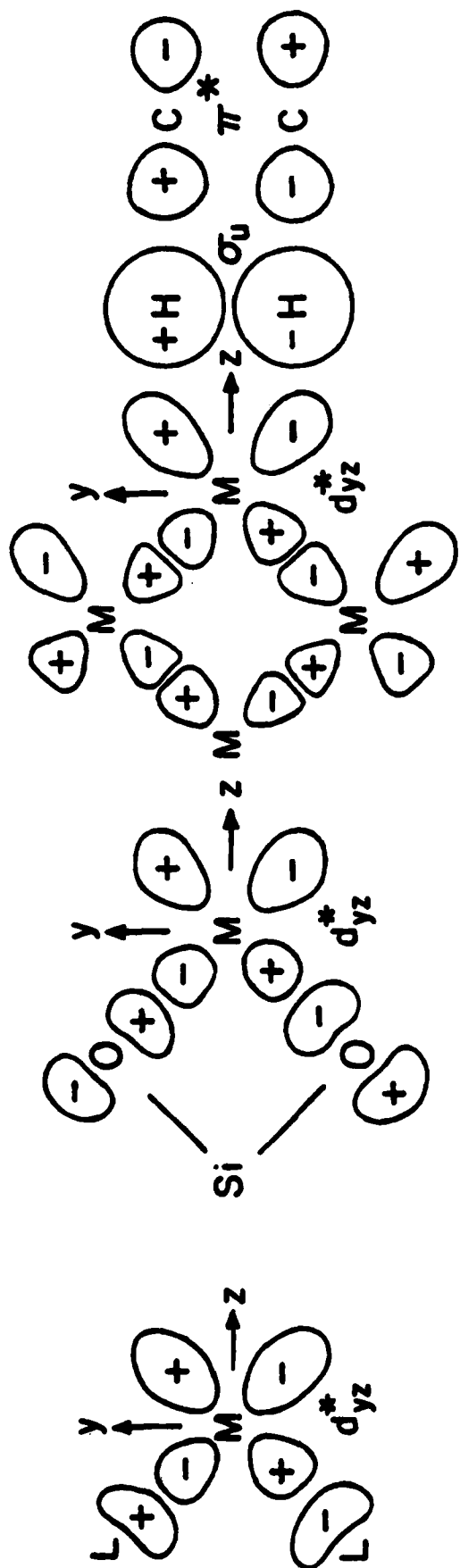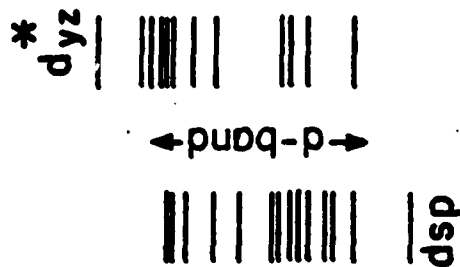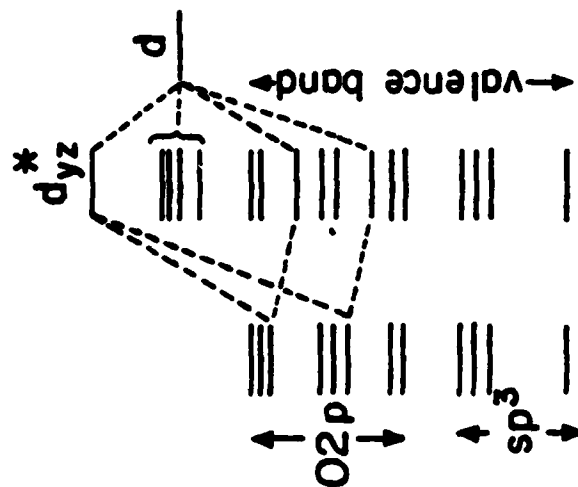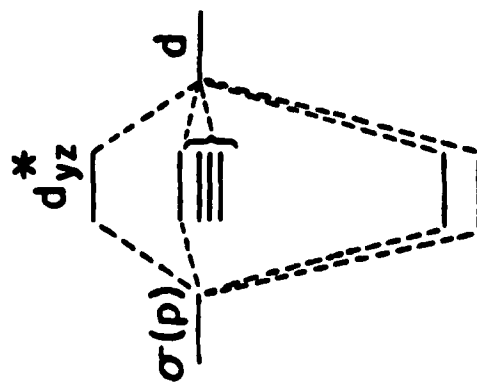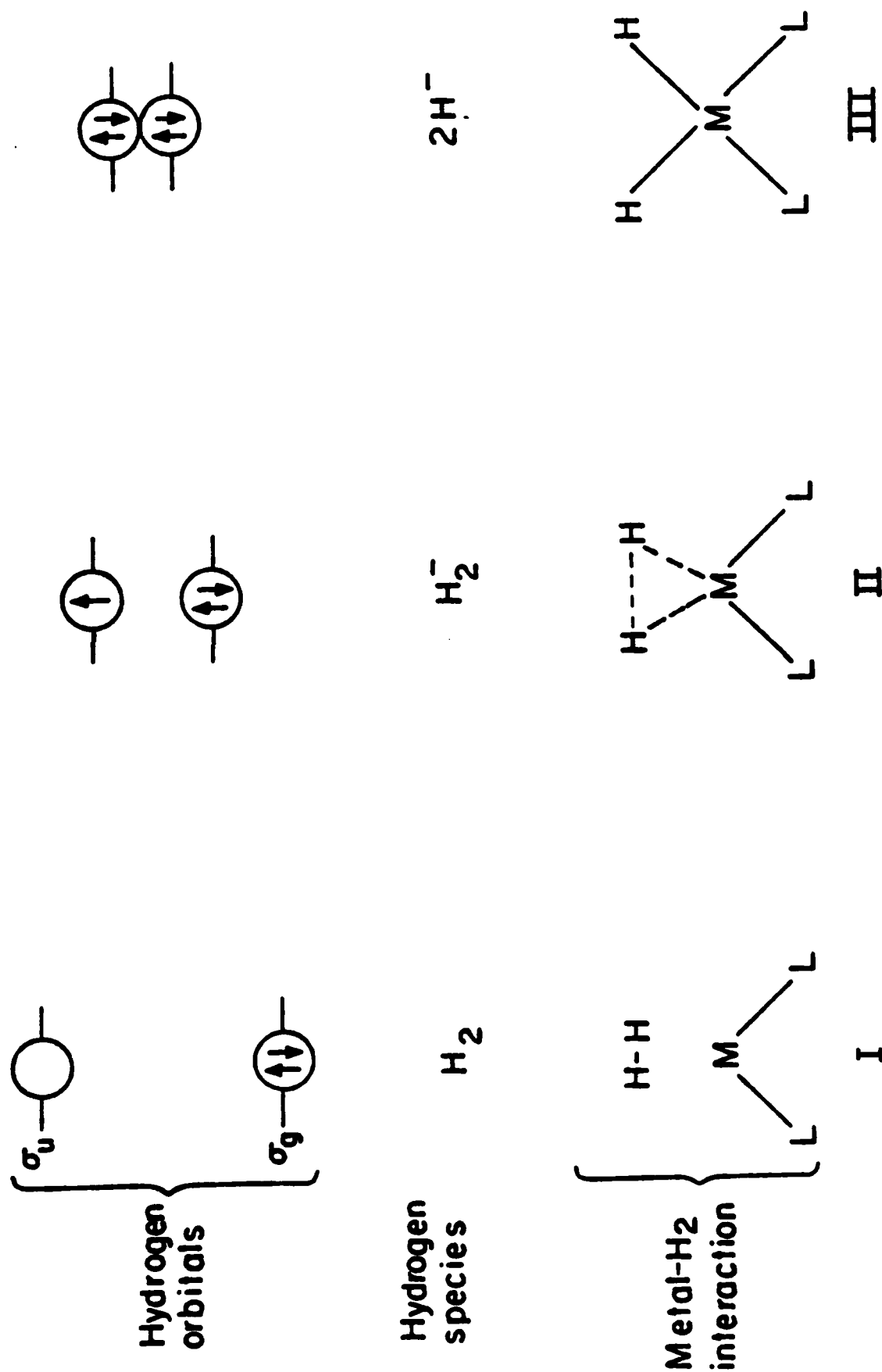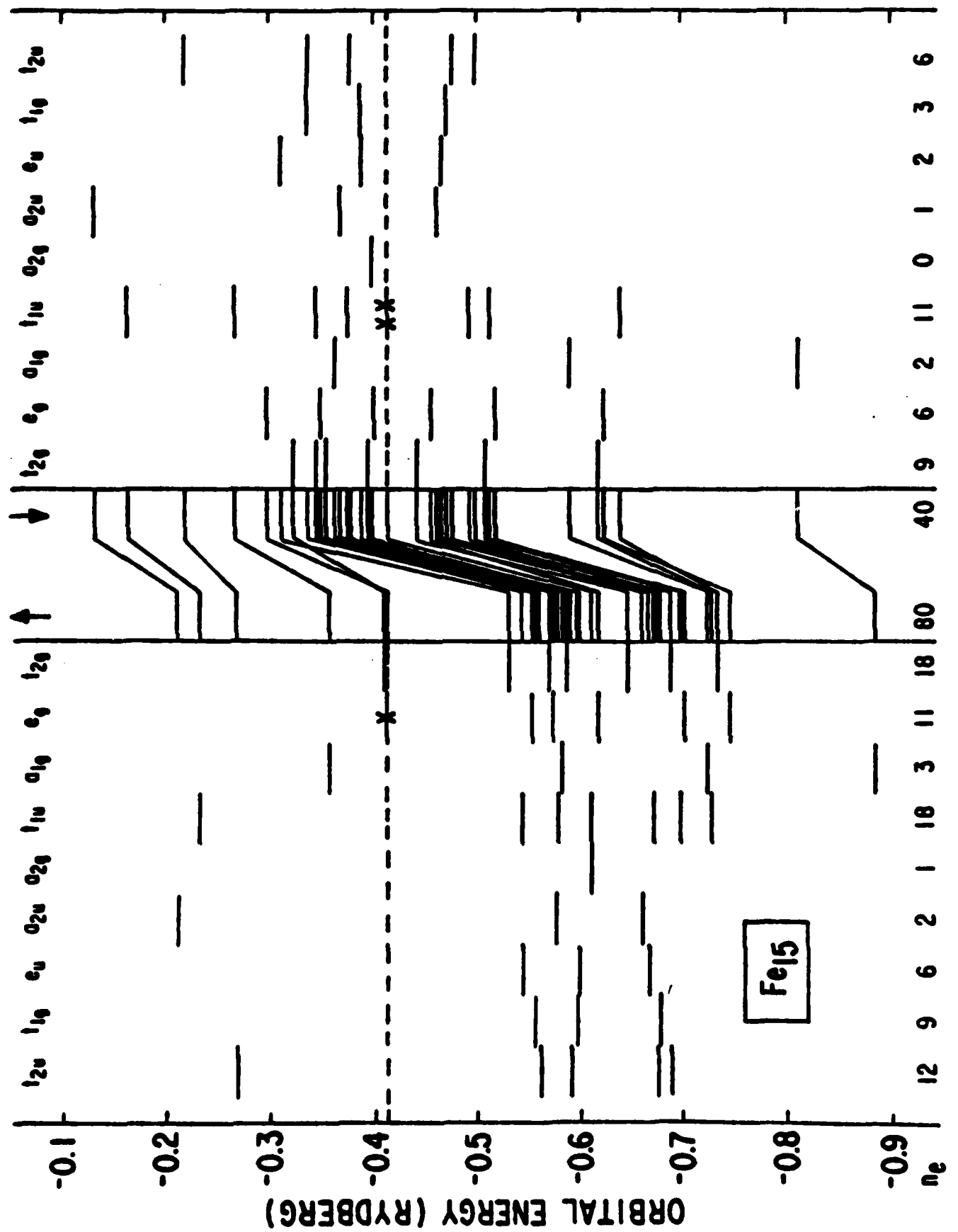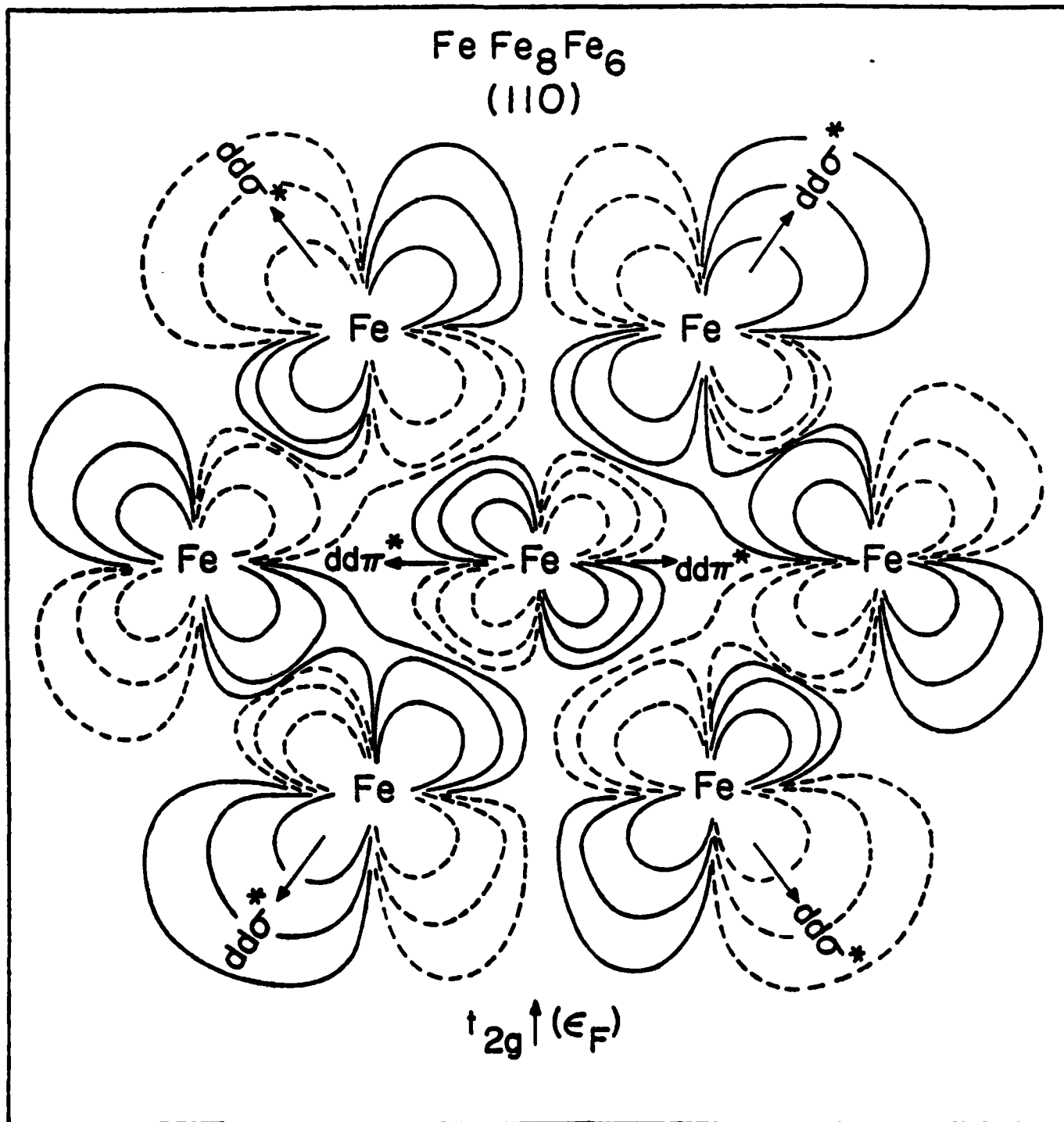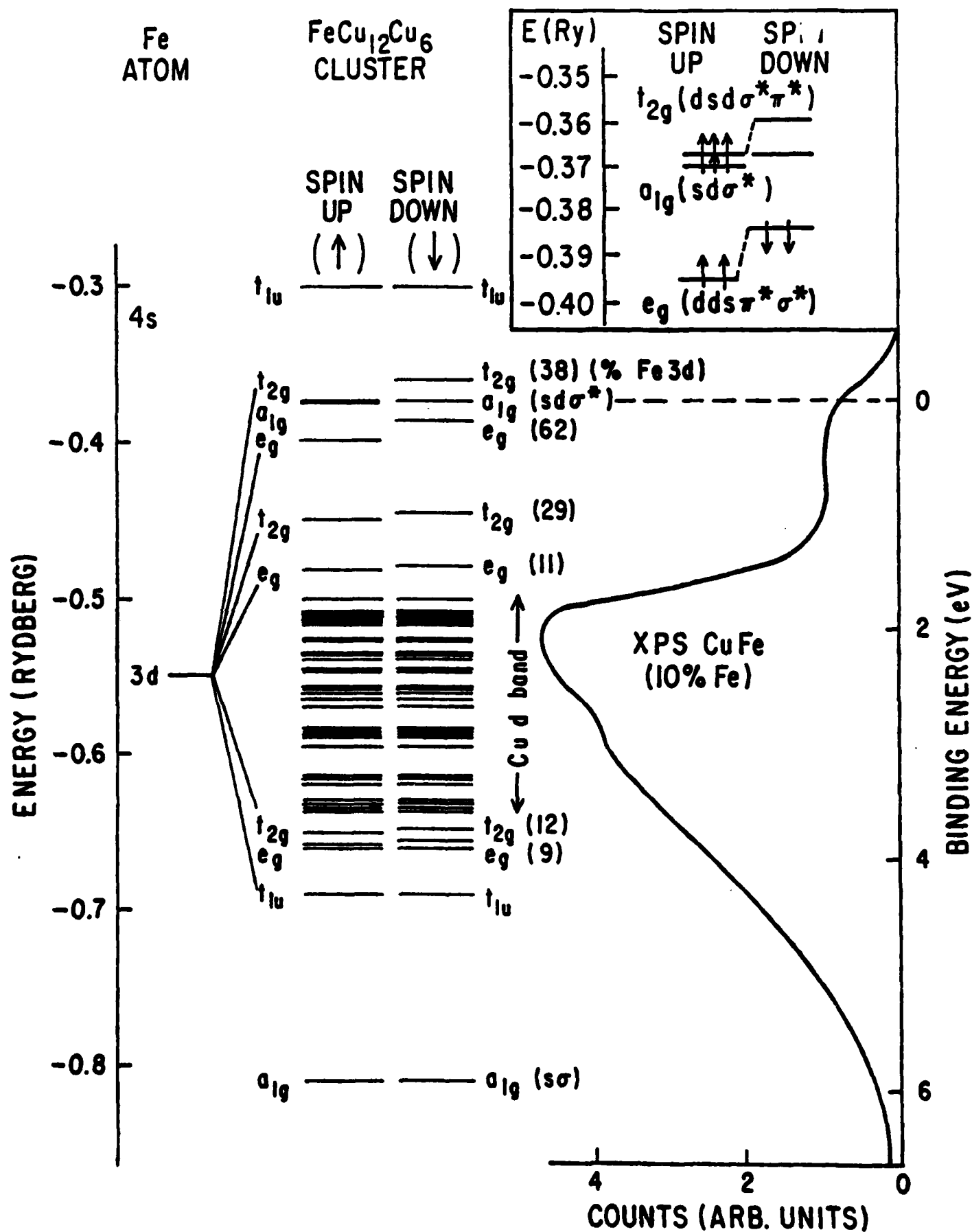
FIGURE 7
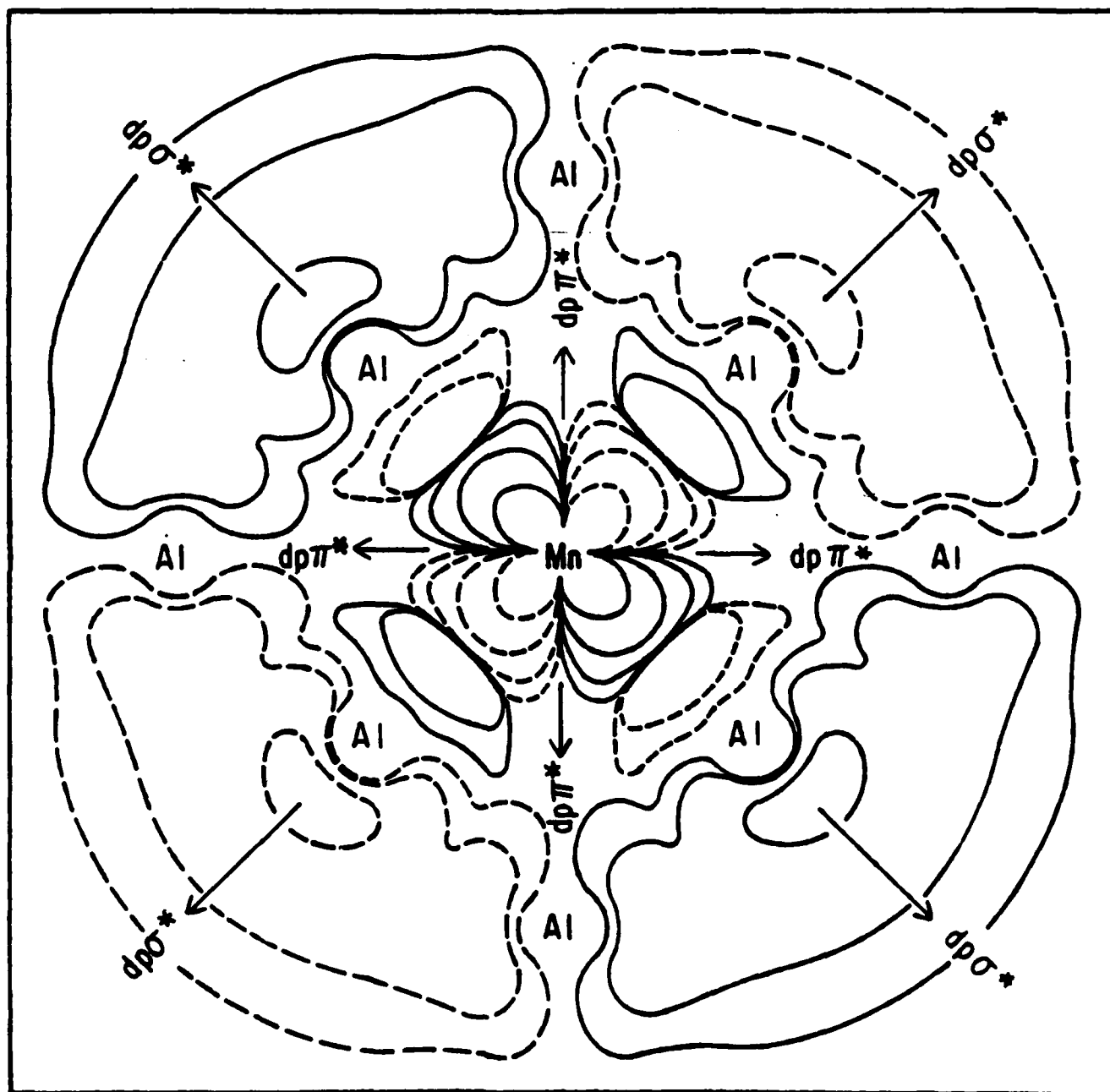
FIGURE 8

FIGURE 9
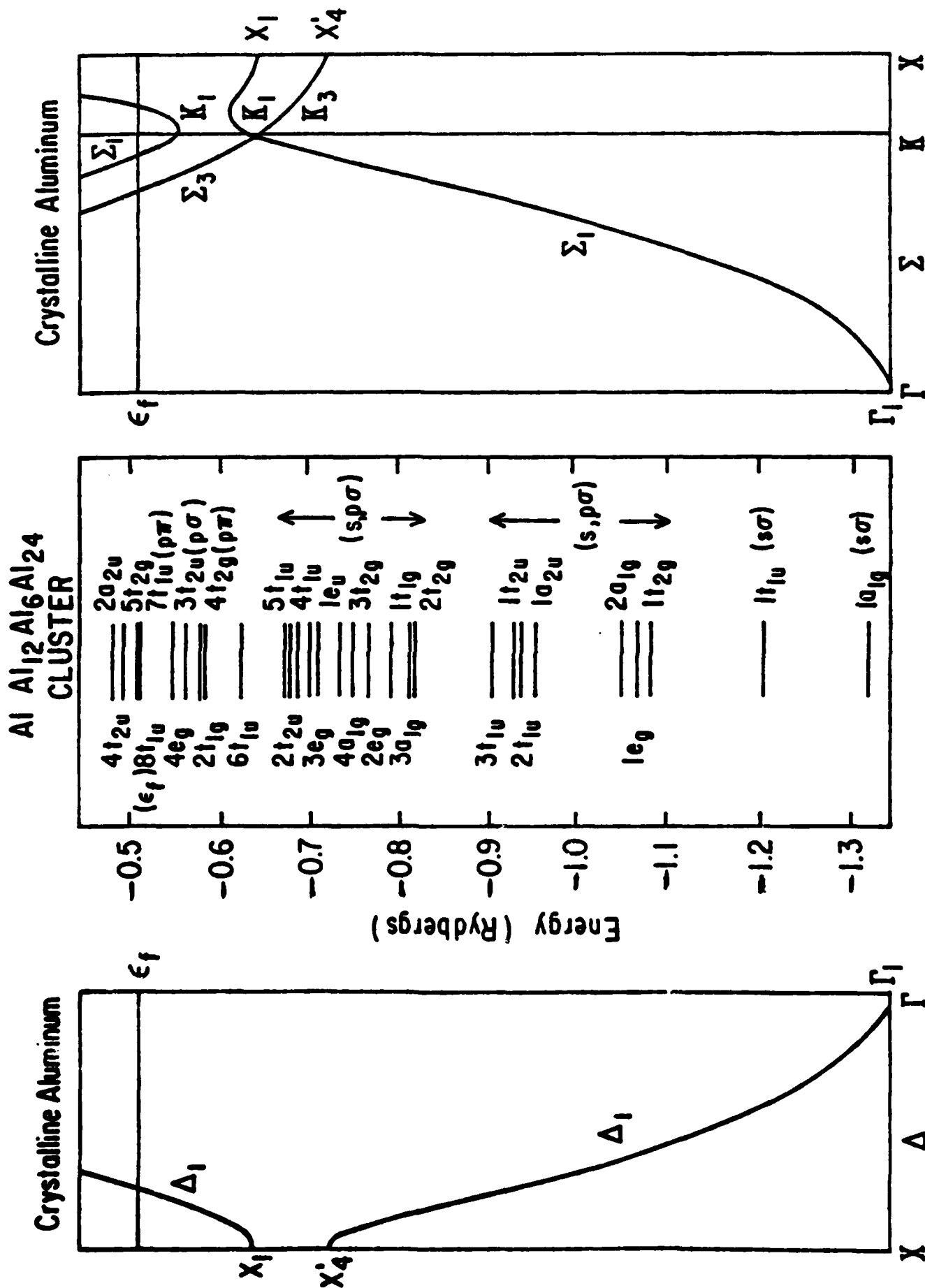
FIGURE 10
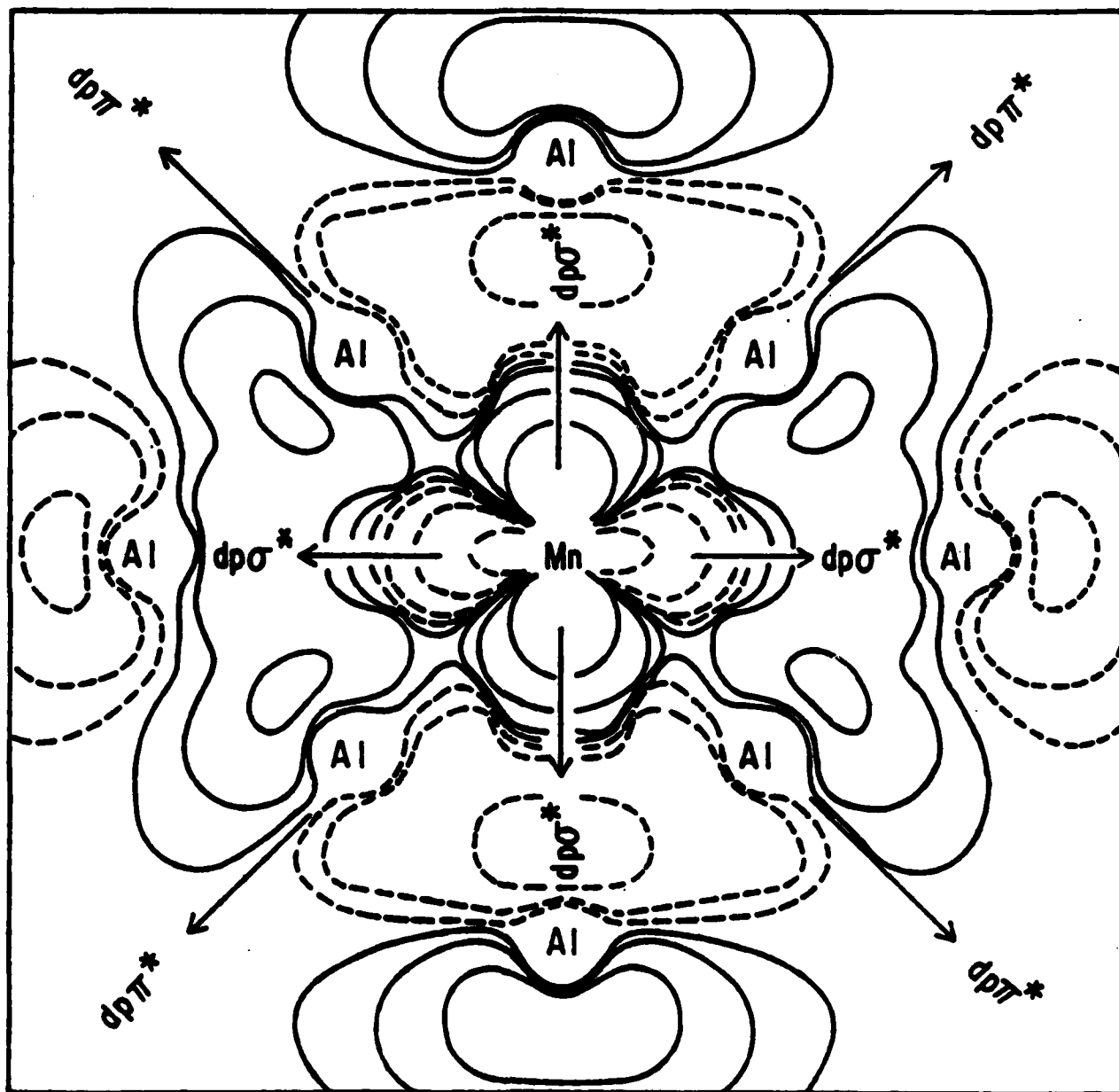
FIGURE 11

FIGURE 12

-40-
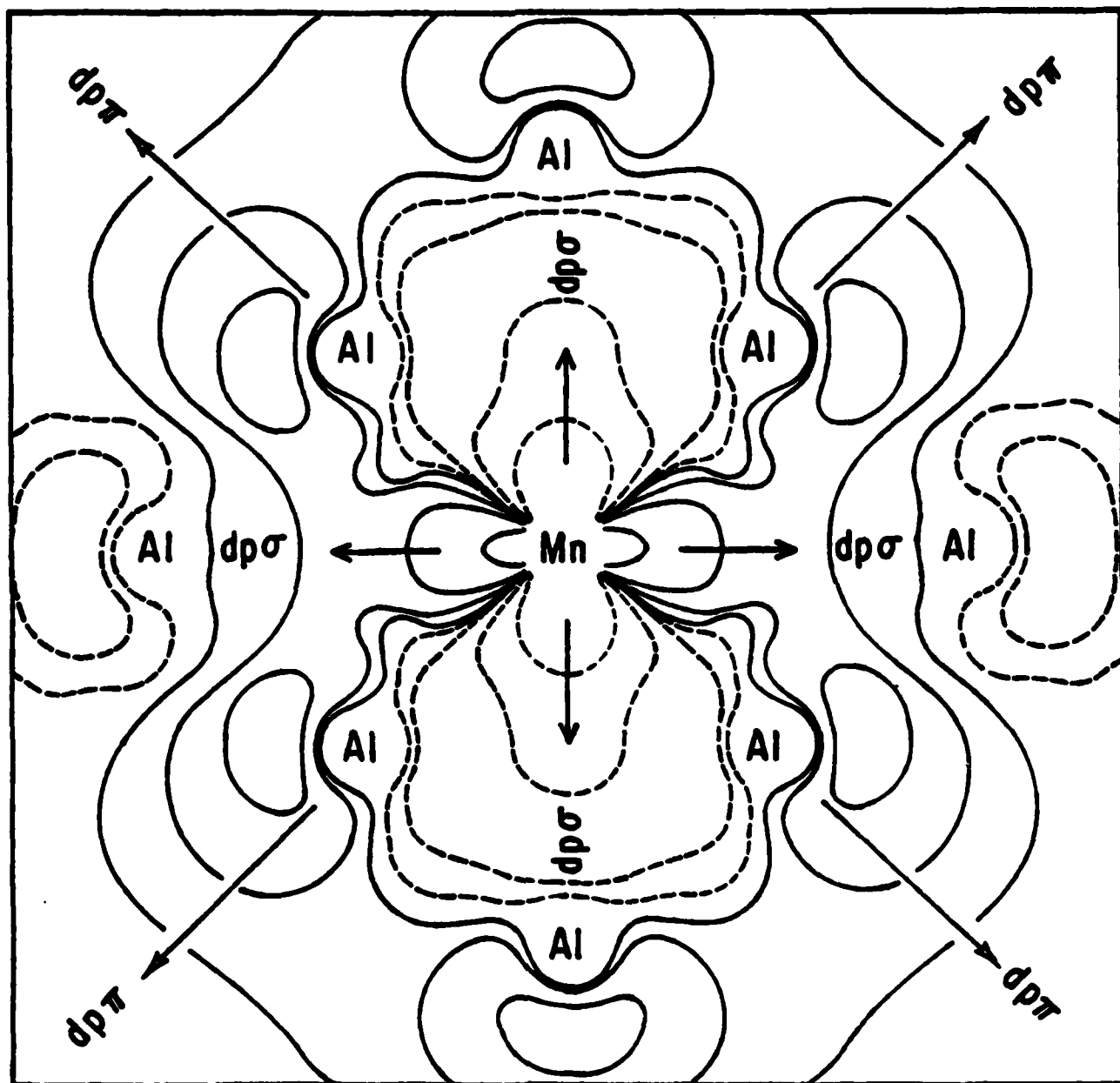
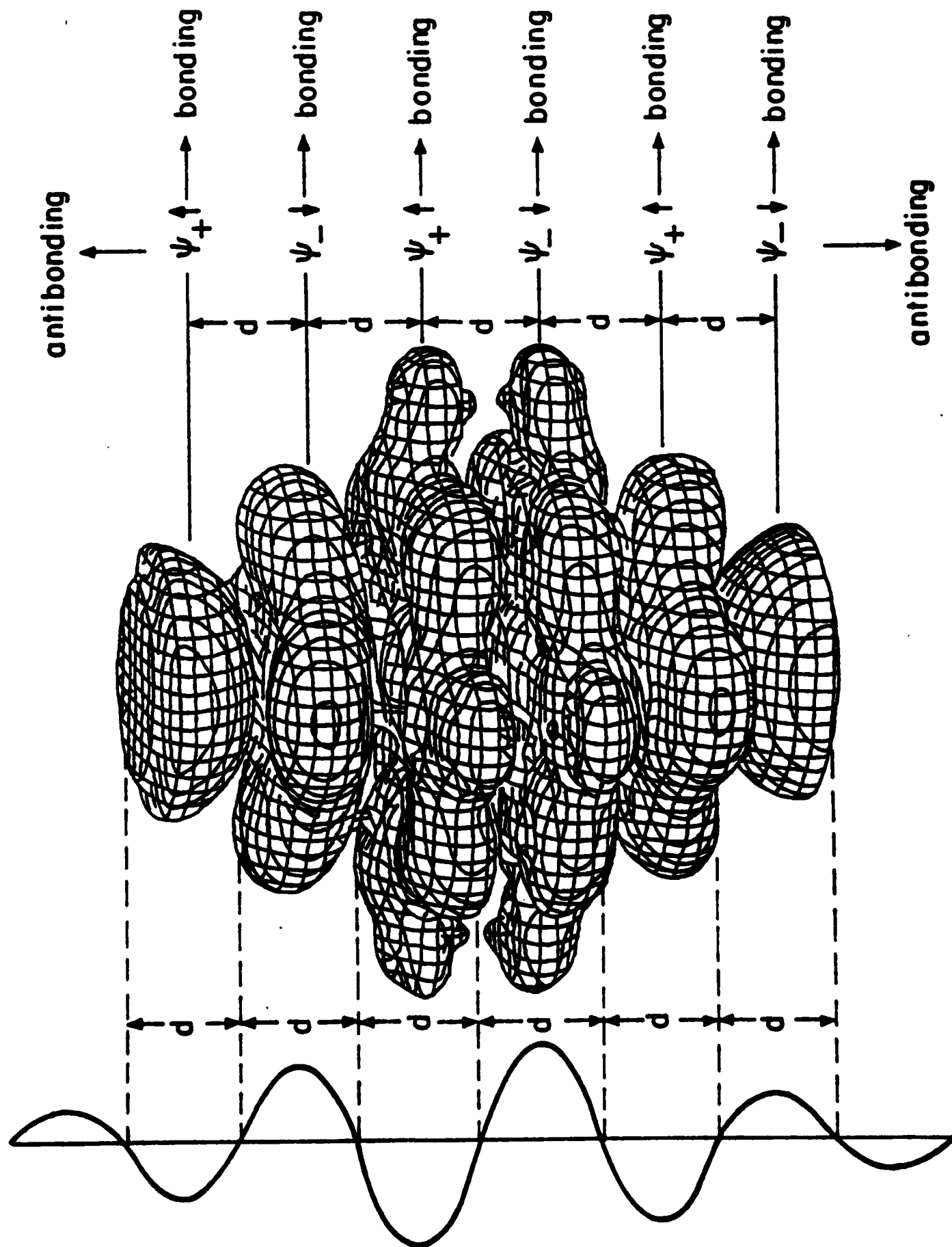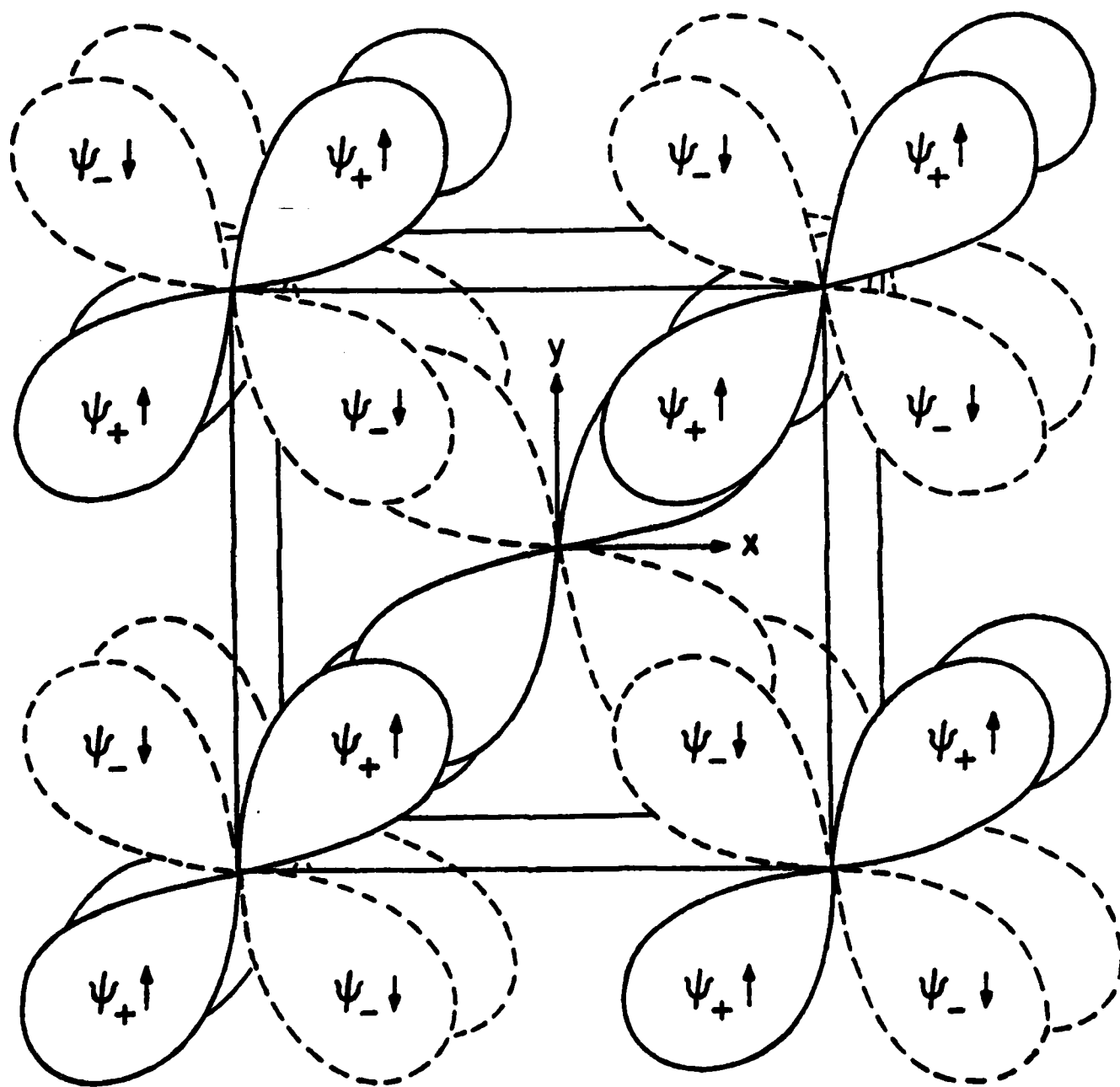FIGURE 13

FIGURE 15

FIGURE 16

FIGURE 17

(a)

(b)

FIGURE 18

-46-

FIGURE 19

$d\delta\,(d_{xy})$

FIGURE 20

-48-

$$d\delta\ (d_{xy})$$

FIGURE 21